

## RESEARCH ARTICLE

10.1002/2016JC011738

## Key Points:

- Numerical mixing is a major part of the total mixing in a high-resolution model of a highly stratified estuary with steep bathymetry
- Model skill is improved by reducing the turbulent mixing to compensate for excessive numerical mixing
- High-resolution observations identify model errors and show that numerical mixing corresponds with regions of observed turbulent mixing

## Correspondence to:

D. Ralston,  
dralston@whoi.edu

## Citation:

Ralston, D. K., G. W. Cowles, W. R. Geyer, and R. C. Holleman (2017), Turbulent and numerical mixing in a salt wedge estuary: Dependence on grid resolution, bottom roughness, and turbulence closure, *J. Geophys. Res. Oceans*, 122, 692–712, doi:10.1002/2016JC011738.

Received 17 FEB 2016

Accepted 12 DEC 2016

Accepted article online 22 DEC 2016

Published online 28 JAN 2017

Corrected 15 MAY 2017

This article was corrected on 15 MAY 2017. See the end of the full text for details.

## Turbulent and numerical mixing in a salt wedge estuary: Dependence on grid resolution, bottom roughness, and turbulence closure

David K. Ralston <sup>1</sup>, Geoffrey W. Cowles <sup>2</sup>, W. Rockwell Geyer <sup>1</sup>, and Rusty C. Holleman <sup>3</sup>

<sup>1</sup>Applied Ocean Physics and Engineering Department, Woods Hole Oceanographic Institution, Woods Hole, Massachusetts, USA, <sup>2</sup>Department of Fisheries Oceanography, University of Massachusetts Dartmouth, New Bedford, Massachusetts, USA, <sup>3</sup>San Francisco Estuary Institute, Richmond, California, USA

**Abstract** The Connecticut River is a tidal salt wedge estuary, where advection of sharp salinity gradients through channel constrictions and over steeply sloping bathymetry leads to spatially heterogeneous stratification and mixing. A 3-D unstructured grid finite-volume hydrodynamic model (FVCOM) was evaluated against shipboard and moored observations, and mixing by both the turbulent closure and numerical diffusion were calculated. Excessive numerical mixing in regions with strong velocities, sharp salinity gradients, and steep bathymetry reduced model skill for salinity. Model calibration was improved by optimizing both the bottom roughness ( $z_0$ ), based on comparison with the barotropic tidal propagation, and the mixing threshold in the turbulence closure (steady state Richardson number,  $Ri_{st}$ ), based on comparison with salinity. Whereas a large body of evidence supports a value of  $Ri_{st} \sim 0.25$ , model skill for salinity improved with  $Ri_{st} \sim 0.1$ . With  $Ri_{st} = 0.25$ , numerical mixing contributed about 1/2 the total mixing, while with  $Ri_{st} = 0.10$  it accounted for  $\sim 2/3$ , but salinity structure was more accurately reproduced. The combined contributions of numerical and turbulent mixing were quantitatively consistent with high-resolution measurements of turbulent mixing. A coarser grid had increased numerical mixing, requiring further reductions in turbulent mixing and greater bed friction to optimize skill. The optimal  $Ri_{st}$  for the fine grid case was closer to 0.25 than for the coarse grid, suggesting that additional grid refinement might correspond with  $Ri_{st}$  approaching the theoretical limit. Numerical mixing is rarely assessed in realistic models, but comparisons with high-resolution observations in this study suggest it is an important factor.

### 1. Introduction

Complex bathymetry, energetic currents, and strong density gradients make estuaries particularly challenging to represent with circulation models. Bathymetric variability directly affects water column dynamics by inducing frontogenesis, lateral circulation, and spatial gradients in mixing and baroclinic forcing [Ralston *et al.*, 2010a; Giddings *et al.*, 2011; Geyer and Ralston, 2015]. To simulate circulation and transport processes, hydrodynamic models must resolve the spatial variability explicitly in the model grid, or else parameterize unresolved processes such as small-scale mixing. For example, turbulence closure schemes are used to parameterize unresolved mixing of momentum and buoyancy due to subgrid scale turbulence, particularly in the vertical dimension. Similarly, parameterization of mixing due to breaking internal waves or bathymetric roughness may be required if these processes are unresolved yet are critical to representing bulk features like stratification or tidal propagation.

In addition to the explicit mixing in models, which is parameterized based on physical processes, numerical discretization of the advection terms in the momentum and transport equations introduces additional, spurious mixing of spatial gradients. For example, a simple one-dimensional case with constant velocity, first-order upwind advection scheme introduces a numerical diffusion coefficient of  $K_{num} = (|u|\Delta x - \Delta t u^2)/2$  [Smolarkiewicz, 1983]. The numerical diffusivity depends on both grid properties ( $\Delta x$ ) and flow velocity ( $u$ ), and both affect the time step ( $\Delta t$ ) through the Courant condition. The numerical diffusion, calculated as  $\partial/\partial x[K_{num}(\partial\psi/\partial x)]$  with  $\psi$  representing salinity, temperature, or another scalar of interest, depends on the numerical diffusivity of the advection scheme as well as the scalar gradients. Higher order advection schemes can reduce the numerical diffusivity or introduce antidiffusive components as means of

minimizing the numerical mixing. Alternatively, numerical mixing can be reduced with higher resolution grids, although in practice grid resolutions are often limited by practical computational constraints. Unstructured grids offer advantages in spatial resolution by allowing concentration of grid cells in featured parts of the domain and greater grid spacing elsewhere [Chen *et al.*, 2007; Huang *et al.*, 2008]. In contrast, structured grids are more restrictive in the allocation of grid resolution but make it easier to implement higher order, and less diffusive, advection schemes, albeit at increased computational cost [Shchepetkin and McWilliams, 1998].

With some exceptions [Rennau and Burchard, 2009; Vitousek and Fringer, 2011; Holleman *et al.*, 2013; Gräwe *et al.*, 2015], the effect of numerical mixing on coastal ocean models remains largely unknown or unacknowledged. Here we examine the balance between explicit turbulent mixing and implicit numerical mixing in a highly resolved unstructured grid model of a tidal salt wedge estuary. The tidal salt wedge presents an extreme test for circulation models, with strong horizontal and vertical salinity gradients, strong tidal and river velocities, sharp bathymetric relief, and turbulent mixing by both boundary layer and internal shear layer processes. These same features—sharp gradients that evolve rapidly—make characterizing conditions in such systems observationally challenging. We use high spatial and temporal resolution observations of salinity, velocity, and turbulence fields to identify errors in the model and make adjustments. Model calibration is a multistep process, systematically optimizing bottom roughness and the turbulence closure to satisfy both the barotropic processes and internal mixing. By directly calculating numerical mixing, we find that it is a significant fraction of the total mixing of salinity, but that the model can be calibrated by reducing the turbulent mixing and that the total mixing, numerical plus turbulent, corresponds reasonably well with observations. By jointly accounting for the grid resolution, bottom roughness, and turbulent mixing, model skill can be improved for important properties such as stratification and bed shear stress.

## 2. Methods

### 2.1. Study Location: Connecticut River Estuary

The Connecticut River is the largest source of freshwater discharging into Long Island Sound, with a mean discharge of about  $500 \text{ m}^3 \text{ s}^{-1}$  and spring freshet conditions that exceed  $2000 \text{ m}^3 \text{ s}^{-1}$ . The tidal range at the mouth is 1–1.5 m and is predominantly semidiurnal, and tides propagate approximately 100 km up the river to the dam near Thompsonville, CT. The estuary is relatively shallow, with multiple bedrock constrictions of 300–400 m width and thalweg depths of 10–12 m separated by wider (700–1200 m), shallower regions with maximum depths of 4–6 m. The modest cross-sectional area of the estuary leads to relatively strong velocities due to the river discharge, corresponding to 0.16 and  $0.7 \text{ m s}^{-1}$  for the average flow and typical freshet conditions. As a result of the shallow bathymetry and strong river velocities, the salinity intrusion is relatively short, typically extending only 5–15 km from the mouth. By comparison, the Hudson River is the next major drainage basin to the west and has a similar mean annual discharge, but its deeper bathymetry results in a salinity intrusion that extends 30–100 km from the mouth. Under moderate to high discharge conditions, the Connecticut is a tidal salt wedge characterized by strong horizontal salinity gradients and strong stratification that varies tidally with frontal propagation during flood tides and intense mixing during ebbs [Ralston *et al.*, 2010a]. The Connecticut is dynamically similar to other tidal salt wedge estuaries that span a range of river discharges [Geyer and MacCready, 2014], including the Changjiang [Li *et al.*, 2014], Fraser [Geyer and Farmer, 1989], Skagit [Ralston *et al.*, 2013], and Merrimack [Ralston *et al.*, 2010a] estuaries.

### 2.2. Numerical Model

The Finite Volume Coastal Ocean Model (FVCOM, version 3.2.1) [Chen *et al.*, 2003, 2013] is used here to simulate flow and transport in the Connecticut River and adjacent Long Island Sound. FVCOM has an unstructured grid composed of triangular elements horizontally and sigma layers vertically. The horizontal advection scheme for momentum is a projection-evolution scheme where the interface values are reconstructed using a least squares reconstruction approach [Hubbard, 1999; Kobayashi *et al.*, 1999]. The horizontal advection scheme for salinity is a central difference scheme with limited dissipation to eliminate overshoots. The vertical advection schemes for both momentum and salinity are central difference. Evaluations of FVCOM with barotropic test cases found overall second-order accuracy for the depth-averaged momentum and continuity equations [Huang *et al.*, 2008]. In applications with irregular coastlines or

complex bathymetry, the unstructured approach allows finer grid resolution compared with structured grid models at similar computational effort, and consequently the second-order advection scheme can provide accuracy similar to higher order advection schemes on coarser grids [Chen *et al.*, 2007; Huang *et al.*, 2008]. FVCOM has been previously applied and evaluated quantitatively in shallow, stratified estuaries such as the Satilla River [Chen *et al.*, 2008], Merrimack River [Ralston *et al.*, 2010a], Skagit River [Ralston *et al.*, 2013], and Pearl River [Lai *et al.*, 2015].

For turbulence closure, FVCOM incorporates the General Ocean Turbulence Model (GOTM, version 4.0.0) [Umlauf and Burchard, 2005]. GOTM allows selection from a range of turbulence closure options, and for these simulations we used the dynamic k-epsilon model with algebraic second-order closure coefficients from Cheng *et al.* [2002]. For the k-epsilon model [Burchard and Bolding, 2001] and other turbulence closures [Burchard, 2001; Umlauf *et al.*, 2003], mixed layer deepening for homogeneous, stratified shear flow can be shown to depend almost entirely on the value of steady state Richardson number ( $Ri_{st}$ ).  $Ri_{st}$  represents the gradient Richardson number ( $Ri_g$ ) at which turbulence has stationary solutions in homogenous shear flow conditions; balanced turbulence grows exponentially for  $Ri_g < Ri_{st}$ , and it decays exponentially for  $Ri_g > Ri_{st}$  [Umlauf *et al.*, 2003]. In laboratory experiments,  $Ri_{st}$  has been found to be around 0.25 [Rohr *et al.*, 1988], consistent with stability theory [Miles, 1961], although reported values span the range  $0.15 < Ri_{st} < 0.25$  [Umlauf *et al.*, 2003]. Lower values of  $Ri_{st}$  result in less mixing, or in the case of a deepening mixed layer, a slower entrainment rate [Burchard and Bolding, 2001]. Equilibrium second-order models also have a critical Richardson number ( $Ri_{cr} > Ri_{st}$ ) above which turbulence is extinguished in homogenous shear layers [Burchard and Bolding, 2001]. For the Cheng *et al.* [2002] stability coefficients,  $Ri_{cr} = 0.96$  [Umlauf and Burchard, 2005]. For comparison with other commonly used algebraic second-order closures,  $Ri_{cr} = 0.24$  for Kantha and Clayson [1994] and  $Ri_{cr} = 0.84$  for version A of Canuto *et al.* [2001].

Numerical mixing results from discretization errors in the tracer advection scheme, and to assess the role of numerical mixing we have integrated the diagnostic approach developed by Burchard and Rennau [2008] into FVCOM. The numerical mixing, defined by the decrease in salinity variance induced by the advection step, is the difference between the advected square of the salinity and the squared salinity after advection divided by the time step:

$$D_{num} = \frac{A\{s^2\} - A\{s\}^2}{\Delta t} \quad (1)$$

where  $s$  is salinity,  $A\{\}$  is the advection operator (e.g., first-order upstream, second-order centered difference), and the  $\Delta t$  is the model time step. The approach combines both vertical and horizontal advection, and the numerical mixing can be positive or negative (i.e., antidiffusive), depending on the advection scheme. The numerical mixing is specific to each tracer field, and can be compared with the physical mixing imposed by the eddy diffusivities from the turbulence closure. The turbulent mixing, or dissipation of salinity variance due to subgrid scale motions, is calculated directly in the model with

$$D_{turb} = 2K_v \left(\frac{\partial s}{\partial z}\right)^2 + 2K_h \left(\frac{\partial s}{\partial x}\right)^2 + 2K_h \left(\frac{\partial s}{\partial y}\right)^2 \quad (2)$$

where  $K_v$  and  $K_h$  are the vertical and horizontal diffusivities. The vertical diffusivity is determined based on the turbulent velocity and length scales, which are calculated by GOTM based on the water column shear and stratification. In these simulations, the explicit horizontal mixing has been removed by setting  $K_h = 0$ , so it does not contribute to  $D_{turb}$ . The turbulent and numerical mixing were calculated at each time step in the model and then saved as averages over the interval between model outputs (every 30 min) to average over temporal oscillations. Note both  $D_{num}$  and  $D_{turb}$  have units of  $\text{psu}^2/\text{s}$ , and are not diffusivity coefficients but rather represent mixing rates, or the decrease in salinity variance over time.

The numerical mixing depends on the scalar gradients, grid resolution, and advection scheme. A previous study of a coastal domain with terrain-following coordinates found that numerical mixing was greatest at sharp scalar gradients in regions of steeply sloping bathymetry, which was where the tracer fields were advected across sigma levels [Rennau and Burchard, 2009]. Other approaches to assess directly the contribution of numerical mixing have also found that it can be a dominant component of mixing in realistic coastal models. A recent method analyzing discrete variance decay reduced the noise in the local estimates, but

found total numerical mixing results consistent with the approach used here [Klingbeil *et al.*, 2014]. Similarly, the numerical dispersion in a nonhydrostatic model was found to be greater than the physical dispersion when grid spacing was greater than the depth to the internal interface, presenting a significant grid resolution requirement for modeling nonhydrostatic processes in realistic domains [Vitousek and Fringer, 2011]. In addition to grid spacing, grid orientation can affect numerical mixing, as aligning unstructured grid cells with the local dominant flow direction has been shown to reduce the lateral diffusion in both idealized and realistic simulations [Holleman *et al.*, 2013].

Simulations of the Connecticut were conducted using two model grids that differed in the number of elements by about a factor of 5. The finer resolution grid had about 110,000 nodes and 210,000 cells, with a typical horizontal resolution in the estuary of about 15 m. The coarser resolution grid had about 23,000 nodes and 42,000 elements with a resolution in the estuary of about 45 m. The grids had the same spatial extent including Long Island Sound and the Connecticut River to the head of tides. Grid resolution decreased with distance from the estuary, so the estuary accounted for about 1% of the total area but 55% (coarse grid) or 70% (fine) of the total nodes. Both grids were run with 30 sigma layers vertically; results were similar for cases run with 40 sigma layers.

Model bathymetry was constructed using existing data sources and new surveys. Digital elevation maps from the National Geophysical Data Center's U.S. Coastal Relief Model (<https://www.ngdc.noaa.gov/mgg/coastal/crm.html>) and National Ocean Service's (NOS) Estuarine Bathymetry database (<http://estuarinebathymetry.noaa.gov/>) were used for Long Island Sound. In the Connecticut River estuary, NOS soundings were supplemented with high-resolution bathymetric surveys by the USGS Woods Hole Seafloor Mapping group using an interferometric sonar system and real time kinematic GPS [Ackerman *et al.*, 2015]. Additional surveys in shallow regions were conducted with small boats using a single beam altimeter and GPS.

Model boundary conditions included water level at eastern and western boundaries of Long Island Sound, discharge for the Connecticut River, and surface wind stress over the domain. To incorporate both the tidal and subtidal forcing, water levels were taken from observations at NOAA stations (Newport, RI, #8452660, Montauk, NY, #8510560, Kings Point, NY, #8516945) (Figure 1). Connecticut River discharge was collected from the USGS station at Thompsonville, CT (#01184000). Spatially and temporally varying winds were extracted from the North American Mesoscale (NAM) Forecast System 12-km resolution model (<http://nomads.ncep.noaa.gov/index.shtml>) and mapped to the FVCOM grid.

### 2.3. Observations

Several observational data sets were used to assess model skill. The simulations presented here focus on a period during November 2013 corresponding with an intensive moored and shipboard measurement campaign. Moored sensors were deployed 17 October to 24 November 2013 to measure water level, salinity, velocity, and turbidity at multiple locations along the estuary (Figure 1). The naming convention for the mooring stations is by frontal zone (numbered 1–5, from the mouth north) and letter to distinguish multiple stations within a frontal zone. Most moorings had conductivity and temperature (CT) and optical backscatter (OBS) sensors for near-bottom and near-surface salinity and suspended sediment concentrations, as well as pressure sensors for water level. Acoustic Doppler current profilers (ADCPs) measured velocity at a subset of the locations (Figure 1), and velocities were rotated into streamwise coordinates based on the direction of maximum variance. Turbidity measurements from the OBSs were calibrated to suspended sediment concentrations using water samples collected at the moorings during shipboard surveys and processed in the laboratory for total suspended mass. Water level, salinity, and turbidity data were collected from USGS monitoring stations at Old Lyme (#01194796), Essex (#01194750), Middle Haddam (#01193050), and Hartford (#01190070), and water levels from NOAA stations at New London (#8461490), New Haven (#8465705), and Bridgeport (#8467150) (Figure 1).

Shipboard surveys were conducted in the estuary from 4 to 8 November during a period of spring tides and moderate river discharge [Holleman *et al.*, 2016]. Along-channel and across-channel transects using multiple vessels were repeated over a tidal cycle in the frontal zones to characterize the structure of the salinity and velocity fields using profiling CTDs and ADCPs. Water samples were collected from a bottom-triggered Niskin for calibration of an OBS on the profiler.

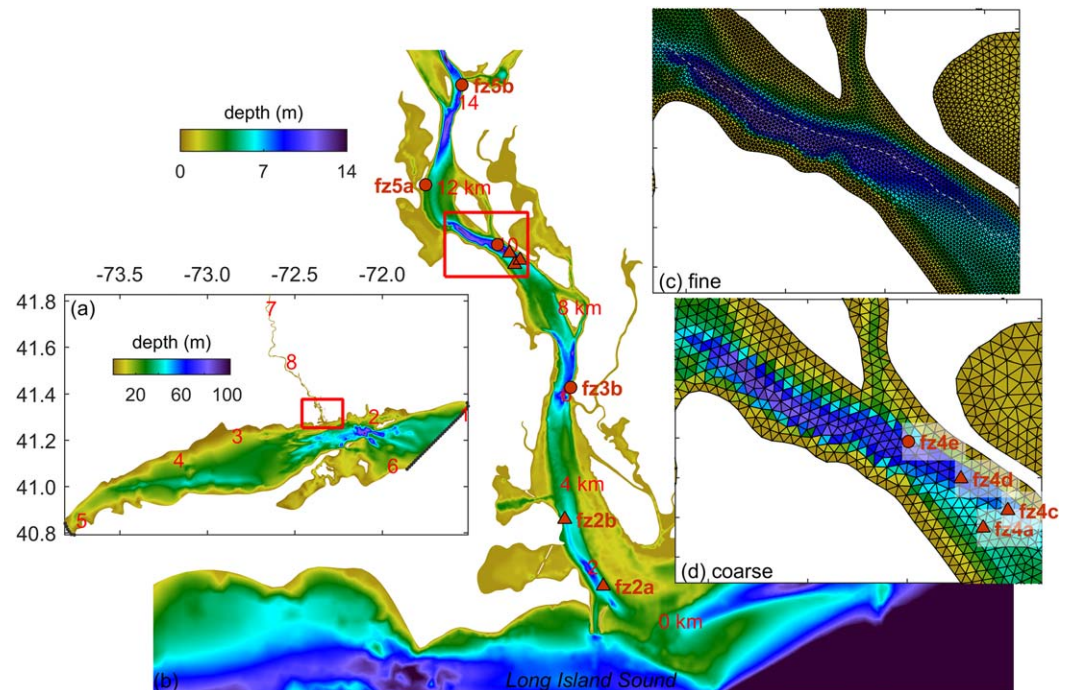


**Figure 1.** The model grid and bathymetry. (a) Model domain including Long Island Sound, with black dots marking open boundaries. Numbered points are locations of water level sensors from NOAA (1. Newport, 2. New London, 3. New Haven, 4. Bridgeport, 5. Kings Point, 6. Montauk) and USGS (7. Hartford, 8. Middle Haddam). (b) Zoom on the Connecticut River estuary, with location shown with red box in Figure 1a. Mooring locations from the observations in November 2013 are labeled, with triangle markers denoting stations with ADCP velocity profilers. Red numbers mark distance along the thalweg from the mouth in km. (c) Zoom on frontal zone 4, showing fine resolution grid along with location of transect in Figures 7 and 8. (d) Zoom on frontal zone 4, showing coarse resolution grid along with mooring locations.

#### 2.4. Model Skill and Optimization

To assess model performance, we calculated skill based on the long-term and intensive mooring data. The model misfit is normalized by the misfit to a reference model, where the reference model is the mean of the observations [Murphy, 1988]; this approach is also termed as model efficiency [Nash and Sutcliffe, 1970]. Specifically,

$$\text{skill} = 1 - \frac{1}{N} \sum_{i=1}^N (x_{o,i} - x_{m,i})^2 / \frac{1}{N} \sum_{i=1}^N (x_{o,i} - \bar{x}_o)^2 \quad (3)$$

where the vector of observations  $x_{o,i}$  contains  $N$  measurements,  $x_{m,i}$  are the model predictions, and an over-bar represents a time average. The maximum skill score is 1, and a skill of 0 has a mean squared error equal to the variance of the observations.

Model calibration was a systematic, multistep process to optimize performance across a range of observed properties. The model must simulate the barotropic flow driven by the tides, river, and wind, and this is predominantly controlled by adjusting the bottom roughness,  $z_0$ . The focus of the skill assessment was on the Connecticut River estuary, but we also compared the model with observed water levels around Long Island Sound and along the length of the tidal Connecticut River. As demonstrated in the results, we found that adjustments to  $z_0$  alone did not resolve important discrepancies between the observations and the model, particularly for stratification and velocity profiles in frontal zones. The salinity distribution is sensitive to mixing, so we adjusted the turbulence closure by changing  $Ri_{st}$ . Previous studies have shown that estuary models are relatively insensitive to the selection of the turbulence closure scheme (e.g., k-epsilon, k-omega, k-kl) [Li et al., 2005; Umlauf and Burchard, 2005; Warner et al., 2005; Wang et al., 2011]. Therefore, we used k-epsilon and systematically adjusted  $Ri_{st}$  to represent the variation in mixing.  $Ri_{st}$  was sequentially reduced, effectively lowering the  $Ri_g$  at which water column shear produced turbulence and mixing, and skill for salinity and velocity was evaluated against observations.

**Table 1.** Calibrated Average  $z_0$  (cm) in the Estuary Depending on  $Ri_{st}$  and Grid Resolution

Grid	$Ri_{st}$				
	0.25	0.15	0.10	0.05	0.02
Fine ( $\Delta x \sim 15$ m)	0.1	0.14	0.21	0.4	0.8
Coarse ( $\Delta x \sim 45$ m)	0.14	0.21	0.4	0.6	0.8

Critically, the optimizations of  $z_0$  and  $Ri_{st}$  are coupled through the effect of stratification on vertical mixing of momentum. With reduced turbulent mixing due to lower  $Ri_{st}$ , the eddy viscosity and eddy diffusivity were reduced and the model was less frictional. Consequently,  $z_0$  had to increase to match the barotropic tidal propagation (see Table 1). The fine and

coarse grid simulations were calibrated separately, resulting in different optimal values for  $z_0$  and  $Ri_{st}$  due to the differences in numerical mixing with grid resolution.

To account for spatial variation in the bottom roughness, we varied  $z_0$  with water depth. Sand waves are an important source of bottom roughness in this system, ranging in height from 0.2 to 1.0 m in the Connecticut River and up to 10 m in eastern Long Island Sound [Bokuniewicz et al., 1977; Horne and Patton, 1989; Patton and Horne, 1992; Knebel et al., 1999]. Observations in eastern Long Island Sound found that maximum sand wave height was limited by water depth, but that in many cases sand wave heights remained well below the proposed limit of  $H = 0.086 d^{1.19}$  [Allen, 1970], where  $H$  is the sand wave height and  $d$  the water depth [Bokuniewicz et al., 1977]. We have simplified this relationship to make  $z_0$  linear with depth and accounted for the factor of 30 between the physical roughness scale and the hydrodynamic roughness [Nikuradse, 1933]:  $z_0 = (d/a_h)/30$ , where  $a_h$  is a scaling factor that is empirically determined by optimizing model skill. For these results,  $a_h$  was between 4 and 32, depending on the grid resolution and turbulence parameterization. The average values for  $z_0$  in the estuary ranged between 0.8 and 0.1 cm. For a reference elevation of 1 m above the bed, this corresponds to drag coefficients ( $C_d$ ) of 0.0069 to 0.0034, greater than the typical  $C_d \approx 0.003$  but consistent with enhanced friction due to bed forms and other unresolved roughness.

### 3. Results

#### 3.1. Salinity and Velocity in the Estuary

In the Connecticut River estuary, the salinity and velocity fields vary significantly at tidal time scales with advection and mixing of the salt wedge. Model results from a simulation during the observation period of November 2013 are used to illustrate typical conditions in the estuary (Figure 2). Observations from vessel-mounted surveys found similar conditions, albeit with measurements at lower spatial and temporal resolution. A quantitative assessment of the model performance is addressed in the next section.

During flood tides, the salt wedge advected landward as a bottom salinity front (Figure 2, top plots). The velocity structure had a relatively thick bottom boundary layer, with a subsurface velocity maximum near the pycnocline [Geyer and Farmer, 1989; Stacey and Ralston, 2005]. The water column was well mixed in the bottom boundary layer, and stratification created by the subsurface velocity maximum was limited. The salinity and velocity fields were laterally variable, with greater landward velocities in the channel. Surface fronts developed, consistent with tidal intrusion fronts [Simpson and Nunes, 1981].

During ebb tides, bottom salinity fronts formed simultaneously at multiple channel expansions along the estuary, as described in the Connecticut by Holleman et al. [2016]; also see Geyer and Ralston [2015]. The fronts produced strong stratification and strongly sheared velocities, with the pycnocline sloping down landward in opposition to the barotropic pressure gradient so that the surface layer ebbed at  $>1$  m  $s^{-1}$  while the lower layer was nearly motionless or continued to flood landward (Figure 2, bottom plots). Five frontal zone (fz) regions are referred to by number with distance from the mouth, from fz#1 at the mouth to fz#5 near the limit of the salinity intrusion during moderate discharge conditions. Shear instabilities at the pycnocline produced mixing in the middle of the water column during ebbs, with  $Ri_g$  typically near 0.25 and mixing efficiencies  $> 0.2$  [Holleman et al., 2016]. The pycnocline and shear layer moved downward during ebbs and depending on the strength of the tidal forcing, the internal shear layer mixing often transitioned to bottom boundary layer mixing, leading to lower  $Ri_g$  and lower mixing efficiencies [Holleman et al., 2016]. For the moderate discharge conditions in November 2013, the bottom salinity fronts typically became entirely mixed by the end of ebb during spring tides, but during neap tides mixing was less complete and high salinity water remained in the deeper parts of the channel after ebbs.

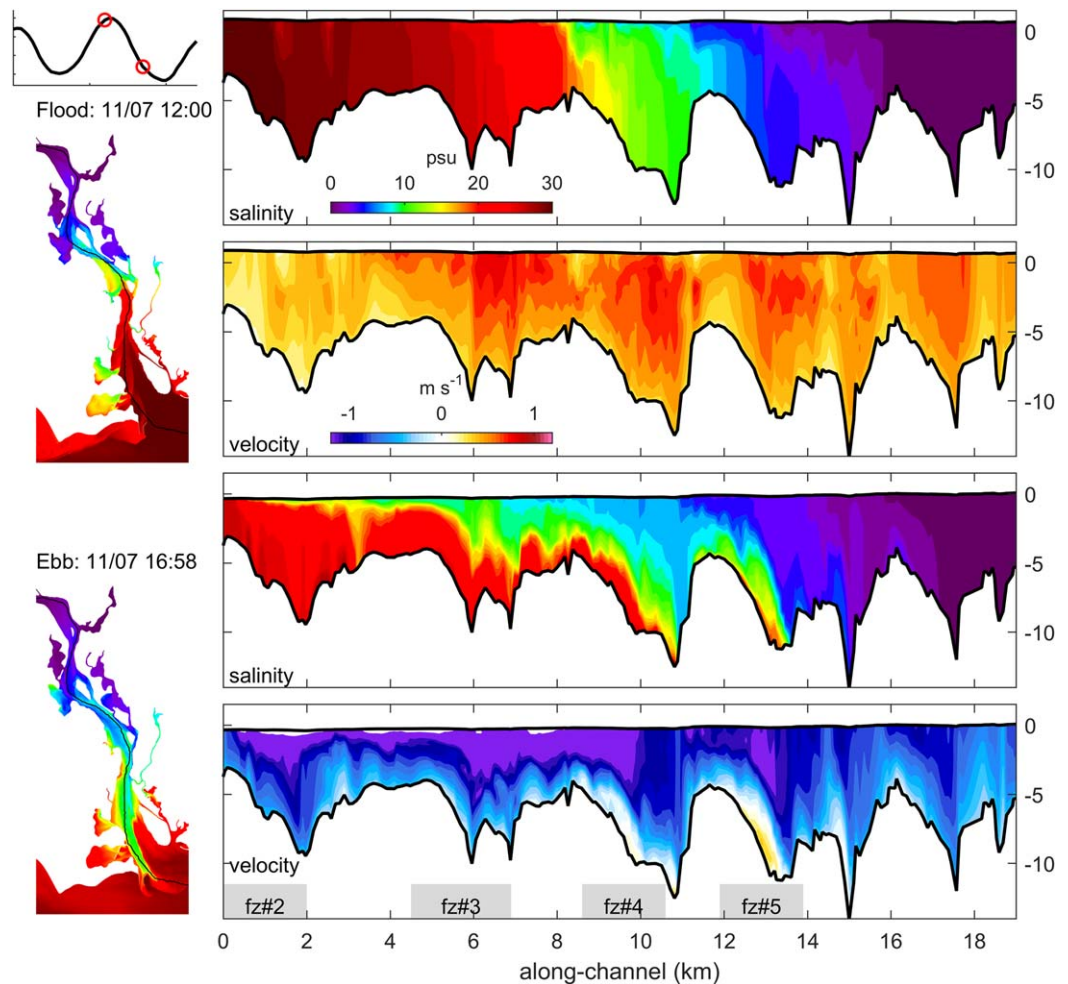


**Figure 2.** Along-channel sections of salinity and along-channel velocity from the fine grid model during the November 2013 observation period. Top plots are during a flood tide and bottom during an ebb. Corresponding surface salinity maps are to the left, marking the location of the along-channel transect. The water level at the time of the two snapshots is shown at the top left.

Time series observations from the moorings recorded the rapid variability in salinity, stratification, and velocity associated with advection of the salt wedge (Figure 3). In the upper estuary (e.g., fz4d), bottom salinity increased from 0 to 25 psu over a couple of hours each flood, and then remained constant until midway through the ebb as the pycnocline moved down in the water column, decreasing only as the front was eventually mixed away. Surface salinity increased after the arrival of the bottom salinity front, but then decreased as the surface layer turned to ebb before the lower layer, enhancing stratification. In the lower estuary (e.g., fz2b), the bottom salinity increased to 30 psu with the passage of the front during floods followed by an extended period with little change. Surface salinity lagged the bottom, and stratification decreased with the passage of the tidal intrusion front during the flood. During ebbs, bottom salinity fronts formed at multiple constrictions along the estuary, increasing stratification. The minimum salinity at the end of the ebbs in the lower estuary varied with the forcing, at times decreasing to  $\sim 10$  psu and at others decreasing only a few psu below the flood tide max.

The highly sheared velocities associated with the salinity fronts during ebbs meant that the observed bottom velocities depended on the stratification and near-bottom salinity (Figure 3). During flood tides, the bottom velocities were in phase with the depth-averaged velocities, consistent with a frictional bottom boundary layer. The surface layer turned to ebb before the bottom, as the tilting pycnocline counteracted the seaward barotropic pressure gradient. During ebbs in frontal zones, there were extended periods when the near-bottom velocity was nearly zero despite strongly seaward depth-averaged velocities (Figures 3 and 4).

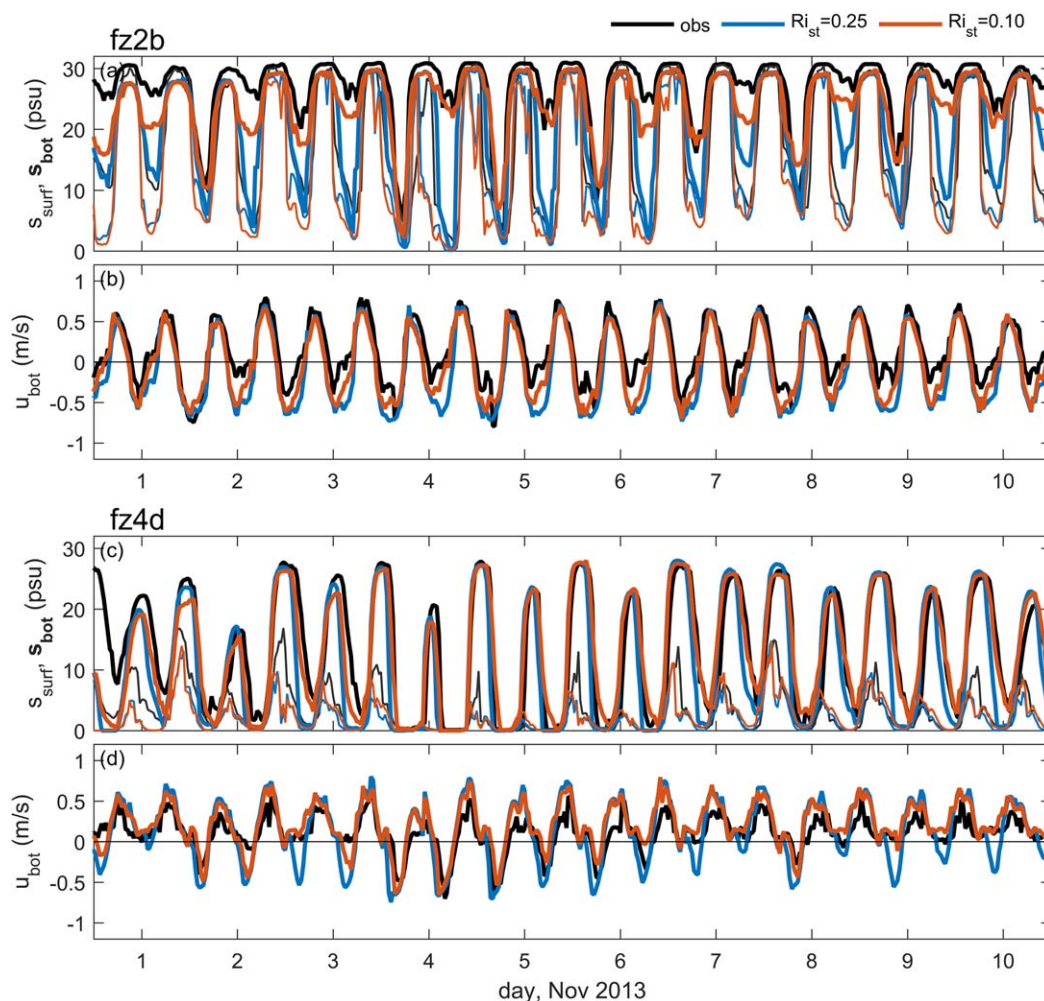


**Figure 3.** Time series of salinity and along-channel velocity from observations and two model cases at two mooring locations during part of the November 2013 observation period. Data are shown from frontal zone 2 (station fz2b) and frontal zone 4 (fz4d), (a and c) surface (thin lines) and bottom (thick lines) salinity and (b and d) near-bottom velocity. The model results are from the fine grid with  $Ri_{st} = 0.25$  (blue) and  $Ri_{st} = 0.10$  (red) in the turbulence closure. Positive velocities are landward.

### 3.2. Calibration and Skill Assessment—Dependence on $z_0$ , $Ri_{st}$ , and Grid Resolution

To calibrate the model,  $z_0$  was progressively adjusted for each case to find the value that yielded the maximum skill for water level and depth-averaged velocity, variables that predominantly depend on the balance between the barotropic pressure gradient and bottom friction, and thus depend on the bottom roughness. The skill assessment was based on the intensive mooring data along with water levels from USGS and NOAA stations in Long Island Sound and the upper Connecticut River. Water levels in Long Island Sound, representing the effects of both tidal and wind forcing, were well represented in the model—skills averaged 0.90 and a ranged between 0.76 and 0.97. Water levels in the tidal, freshwater region of the Connecticut depended on both river discharge and the tidal forcing from downstream. Skills at Middle Haddam (30 km from the mouth) and Hartford (80 km) were 0.77 and 0.53, respectively, and depended on the bottom roughness in the tidal river.

For water level and for depth-averaged velocity in the estuary, the skill scores were excellent for all model cases, between 0.85 and 0.95 (Figure 5). For the fine grid case with  $Ri_{st} = 0.25$ , the average  $z_0$  in the estuary resulting from the calibration was 0.1 cm, or  $C_d = 0.0034$  at 1 m reference height (Table 1). For the coarser grid, also with  $Ri_{st} = 0.25$ , the calibrated bottom roughness was about 50% greater, with  $z_0 = 0.14$  cm, or  $C_d = 0.0037$ . The finer model resolves more of the 3-D structure of the flow, allowing for stronger lateral shears and redistribution of momentum to sinks at the bed or in water column, and consequently the

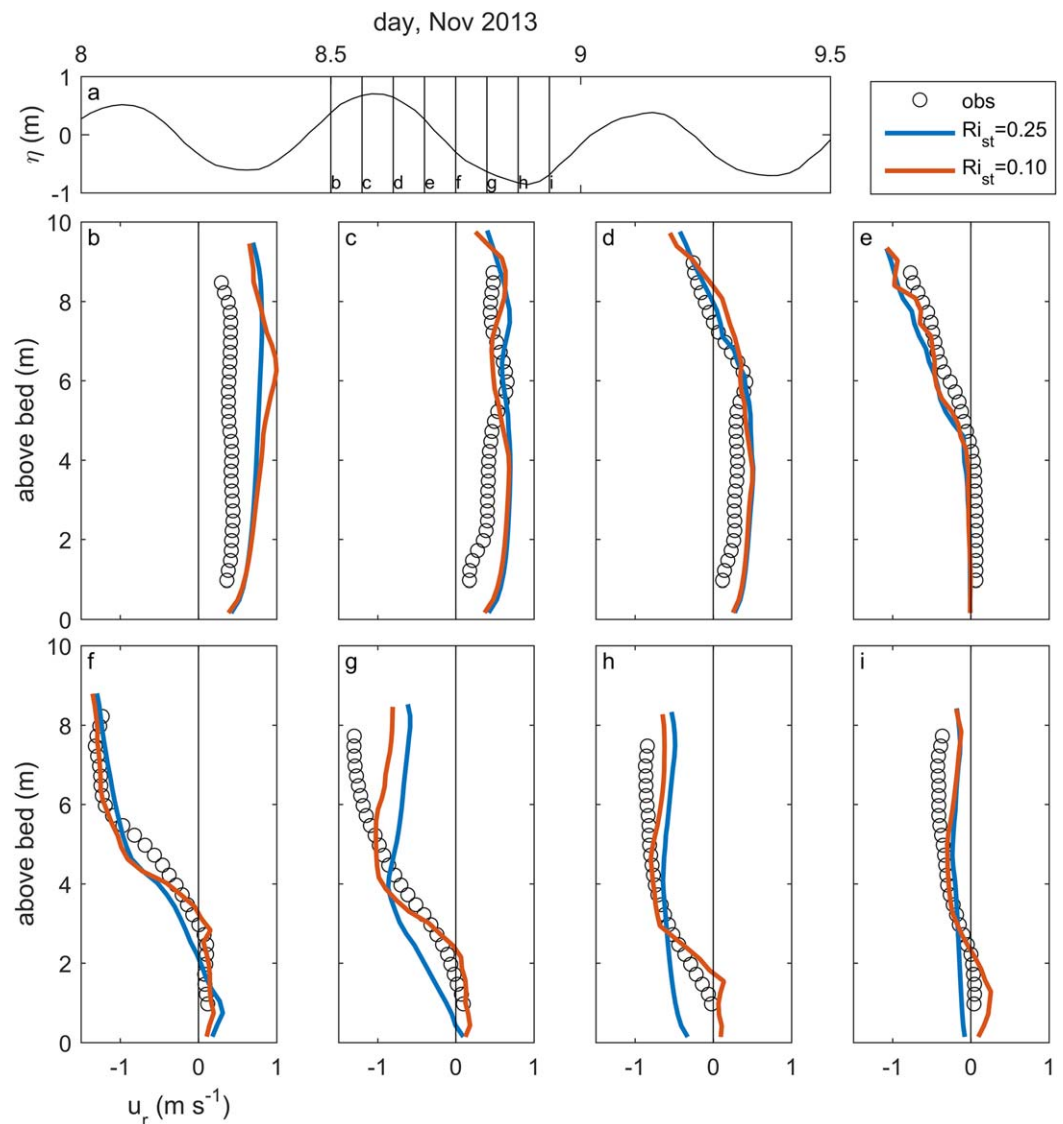


**Figure 4.** Along-channel velocity profiles from frontal zone 4 (station fz4d) over a tidal cycle. (a) Water level with times of velocity profiles marked. (b–i) Observed (ADCP) and modeled velocity profiles from the fine grid with  $Ri_{st} = 0.25$  (blue) and  $Ri_{st} = 0.10$  (red). Positive velocities are landward.

coarser grid requires a greater  $z_0$  to achieve the same loss of tidal energy. The optimal  $z_0$  for the coarser grid was also greater than the finer grid for the other turbulent mixing cases ( $Ri_{st}$ ), typically by a factor of about 50%.

The near-bottom velocity and salinity skills had greater discrepancies between the model and the observations, and among the model cases, than the barotropic quantities. Skill for near-bottom quantities decreased with distance from the mouth, indicative of the representation of the position of bottom salinity fronts during ebbs. Near-bottom velocity skills ranged from  $>0.8$  near the mouth to  $0.5$ – $0.7$  at the more landward stations to around  $0$  in the thalweg of frontal zone 4 (Figure 5). Within frontal zone 4, skills were greater on the shoals ( $0.8$  at fz4a) than in the thalweg, and decreased toward the landward limit of the front. Similarly, bottom salinity skills decreased along the estuary, and were greater on the shoals than in the channel. Bottom salinity skills were also modest ( $0$ – $0.5$ ) in frontal zone 2 due to the curving, steeply sloping channel and strong velocities, as will be examined later in greater detail.

The fine grid cases were run using a range of  $Ri_{st}$  to test the sensitivity of the results to the mixing by the turbulence closure.  $Ri_{st}$  was set to  $0.25$ ,  $0.15$ ,  $0.10$ ,  $0.05$ , and  $0.02$ , representing an increasing threshold in

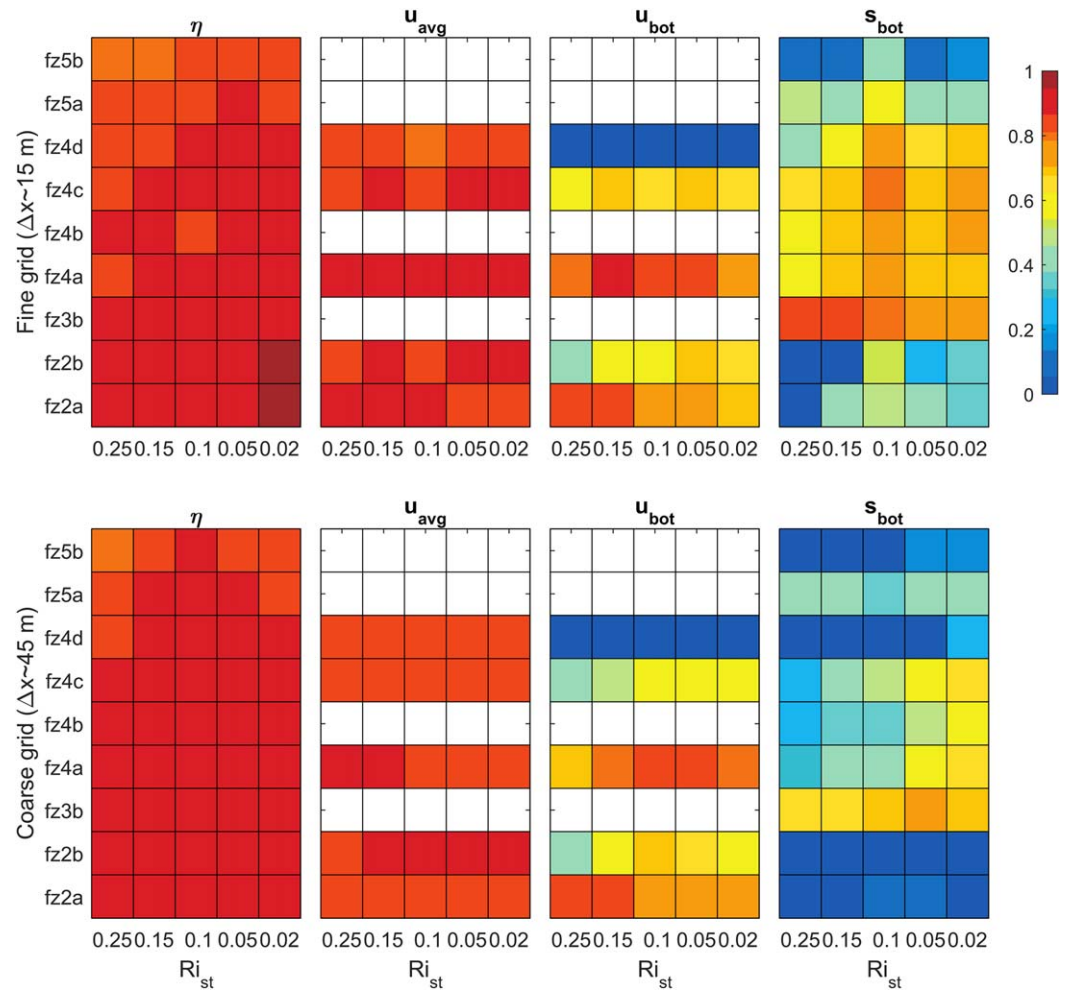


**Figure 5.** Skill scores based on comparison with observed time series from November 2013 for fine grid (top row) and coarse grid (bottom row) model results with  $Ri_{st}$  values of 0.25, 0.15, 0.10, 0.05, and 0.02. Mooring locations are noted on the y axis, and are shown on the map in Figure 1. Skill scores are calculated for water level ( $\eta$ ), depth-averaged velocity ( $u_{avg}$ ), near-bottom velocity ( $u_{bot}$ ), and near-bottom salinity ( $s_{bot}$ ). For each model case,  $z_0$  was optimized to maximize skill scores for a given grid resolution and  $Ri_{st}$ .

shear for mixing by the turbulence closure and a decrease in the mixing rate for a given shear and stratification. Although the smaller values of  $Ri_{st}$  are not consistent with turbulence theory, the associated reduction in resolved mixing may compensate for the excess numerical mixing, thereby yielding higher model skill for the salinity structure than the more physically realistic values of  $Ri_{st}$ . For the water levels and depth-averaged velocities, similarly high skill could be found for any of the  $Ri_{st}$  values provided the  $z_0$  was adjusted in the calibration. Recall that when decreasing  $Ri_{st}$ ,  $z_0$  must increase to compensate for the reduction in frictional losses in the water column (Table 1). For example, for  $Ri_{st} = 0.10$ , the optimal  $z_0$  was 0.21 cm, about twice the value of 0.1 cm for  $Ri_{st} = 0.25$ . While the different turbulence closure cases yielded similar skills for the barotropic quantities of water level and depth-averaged velocity, reduction in  $Ri_{st}$  had a more pronounced positive effect on skill for near-bottom velocity and salinity (Figures 3–5). For the fine grid, the highest skills were with  $Ri_{st} = 0.10$  and  $0.15$ , less than  $Ri_{st}$  from observational and numerical studies (0.15–0.25). Further decreases in  $Ri_{st}$  resulted in lower skills for the fine grid.

The effect of the turbulence closure on the velocity profile is seen in an example tidal cycle from frontal zone 4 (Figure 4). During the flood (Figures 4b–4d), the two cases ( $Ri_{st} = 0.10$  and  $0.25$ ) gave nearly identical results because the dynamics are controlled by the bottom roughness, which was calibrated based on the water level and depth-averaged velocity. During ebbs, the shear layer in the case with greater turbulent mixing ( $Ri_{st} = 0.25$ ) was more diffuse and moved down toward the bed earlier in the ebb (Figures 4f–4h). By the end of the ebb, the near-bottom velocities and bed stresses in the case with  $Ri_{st} = 0.25$  were seaward at

**Table 2.** Error as a Function of Grid Resolution (Mean Spacing in the Estuary), With the Means of the Mean Error (ME) and Root-Mean-Squared Error (RMSE) for All Observations (Seven Stations for Velocity, 10 Stations for Salinity) for Depth-Averaged Velocity, Near-Bottom Velocity, and Near-Bottom Salinity<sup>a</sup>

	Depth-Averaged Velocity		Near-Bottom Velocity		Near-Bottom Salinity	
	ME	RMSE	ME	RMSE	ME	RMSE
$\Delta x = 45$ m $Ri_{st} = 0.25, z_0 = 0.10$ cm	0.070	0.24	0.12	0.29	3.7	7.0
$\Delta x = 15$ m $Ri_{st} = 0.25, z_0 = 0.10$ cm	0.067	0.22	0.095	0.25	2.3	5.3
$\Delta x = 15$ m $Ri_{st} = 0.10, z_0 = 0.21$ cm	0.067	0.22	0.064	0.21	0.71	3.7

<sup>a</sup>Cases listed are the coarse and fine grid with  $Ri_{st} = 0.25$  and average in the estuary  $z_0 = 0.10$  cm (changing only grid resolution), and the fine grid with  $Ri_{st} = 0.10$  and average  $z_0 = 0.21$  cm (calibrating bottom roughness and turbulence closure).

$\sim 0.5 \text{ m s}^{-1}$ , whereas in the case with reduced turbulent mixing ( $Ri_{st} = 0.10$ ) the near-bottom velocities remained near zero, more consistent with the observations.

Model skills for water level and depth-averaged velocities using the coarser grid were comparable to those for the finer grid (Figure 5). Effects of the coarser grid were more apparent for near-bottom velocity and salinity, with lower skill scores than the finer grid. The skills for the coarse grid had similar spatial distribution to the finer grid, decreasing with distance into the estuary and lower skills for bottom salinity in frontal zone 2. The same range of  $Ri_{st}$  was tested for the coarse grid, and the optimal  $z_0$  increased as  $Ri_{st}$  decreased, as with the fine grid (Table 1). For the coarse grid, the  $Ri_{st}$  case with the highest skill scores for the near-bottom quantities was the lowest value of 0.02, indicating the model performance improved when the mixing by the turbulence closure was minimized.

Greater grid resolution is expected to improve model skill regardless of the bottom roughness or turbulence closure. To examine the role of grid resolution alone, a coarse grid simulation was run with the same model parameters as the fine grid case ( $Ri_{st} = 0.25$ , average  $z_0 = 0.10$  cm). In comparisons with observed velocity and salinity, the finer grid did have lower mean and RMS errors than the coarse grid (Table 2). In idealized barotropic test cases, FVCOM was found to have a convergence rate for the root-mean-squared (RMS) error of sea surface elevation that was approximately second order [Huang *et al.*, 2008]. A study using an unstructured grid model (SUNTANS) of North San Francisco Bay found less than the expected second-order convergence for that model [Chua and Fringer, 2011], likely due to errors (e.g., bottom roughness, bathymetric data) that are independent of the discretization error addressed by grid resolution. Comparisons of the fine and coarse grids for the Connecticut also suggest a convergence rate less than second order, but we lack the range of grid resolutions to evaluate it robustly. Reduction in turbulent mixing for the fine grid case ( $Ri_{st} = 0.10$ ) had a negligible effect on the error for depth-averaged velocity, but near-bed salinity and velocity both had marked error reductions (Table 2).

The model characteristics leading to the lower skill scores for near-bottom salinity and velocity as well as the dependence on the turbulence closure settings are illustrated with a comparison to observations in frontal zone 4 during an ebb (Figure 6). Repeated transects approximately every 25 min (every other transect is plotted here) using a tow-yo CTD with casts every 20–40 m detail the sharp spatial gradients and rapid changes in stratification (transect location shown in Figure 1c). In addition to the observations (top plots), we examine three model cases: the finer grid with  $Ri_{st} = 0.25$ , the finer grid with  $Ri_{st} = 0.10$ , and the coarser grid with  $Ri_{st} = 0.02$ , the latter two cases being the turbulence closure settings with the maximum skill for bottom salinity for the respective grid resolutions.

Early in the ebb, the observed pycnocline was sharp ( $N \sim 0.4 \text{ s}^{-1}$ ) and tilted landward approximately parallel to bottom and about 5 m above the bed (Figure 6, top left). During the ebb, the pycnocline moved progressively down and became more diffuse. At the end of the sequence, the pycnocline was limited to the lowest 2 m of the water column, and yet high salinity ( $>20$  psu) water remained in the deepest part of the channel. The model results had more complete coverage, extending upstream to where the bed sloped upward toward broad, shallow shoals. In the fine grid case with  $Ri_{st} = 0.25$ , the evolution of the pycnocline through the ebb was similar to the observations, but with important differences (Figure 6, second row).

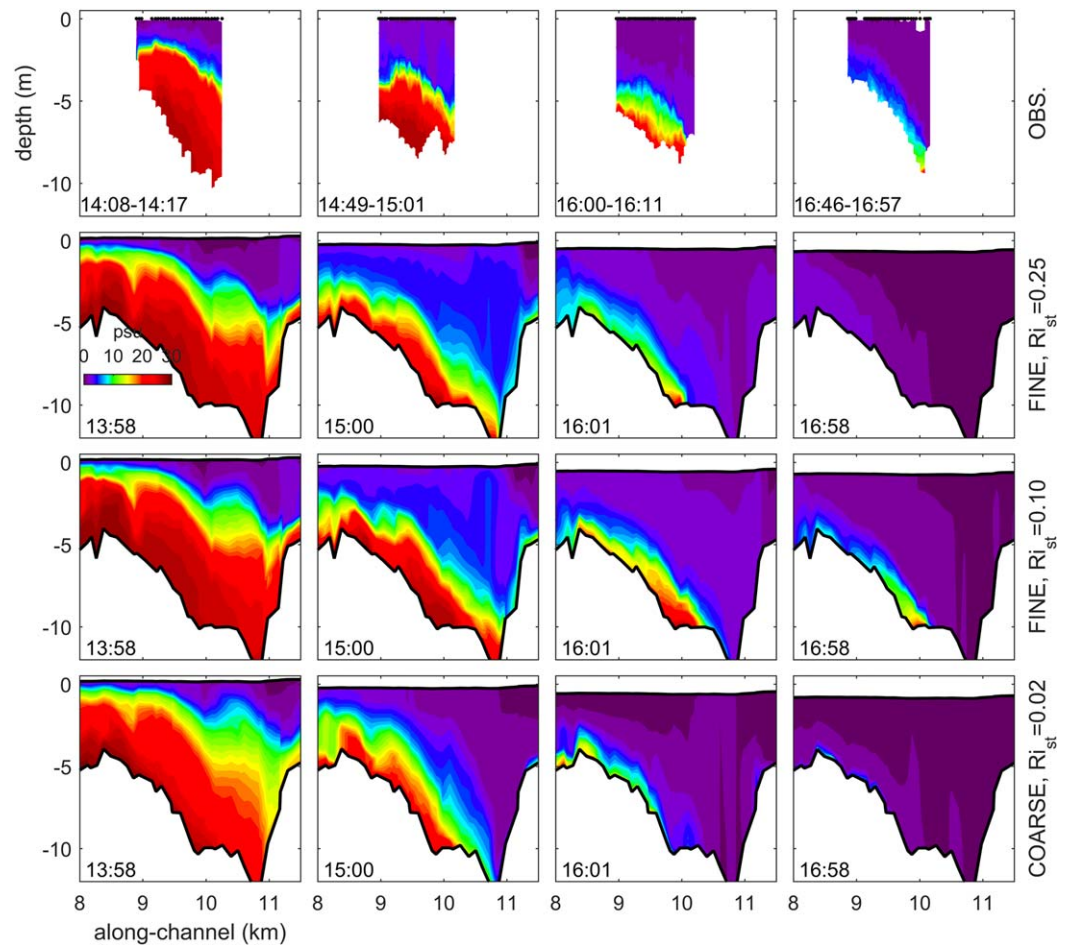


**Figure 6.** Along-channel sections of salinity from frontal zone 4 at four times during an ebb tide on 5 November 2013 from observations (top row) and three model cases at output times closest to the observations. Model cases are from the fine grid with  $Ri_{st} = 0.25$  (second row), the fine grid with  $Ri_{st} = 0.10$  (third row), and the coarse grid with  $Ri_{st} = 0.02$  (fourth row). Times of the sections are shown in the bottom left corner. Markers in top plots show CTD cast locations.

Early in the ebb, the pycnocline was already more diffuse than observations ( $N \sim 0.2 \text{ s}^{-1}$ ), including a layer of intermediate salinity water near the upstream end of the frontal zone. By the end of the ebb, the salinity had been almost completely mixed and expelled from the frontal zone. In the coarse grid case with low turbulent mixing ( $Ri_{st} = 0.02$ ), the results were similar—a thicker pycnocline, particularly at the upstream end, and destruction of the salinity front by the end of the ebb (Figure 6, fourth row). The excessive mixing and loss of the salinity front corresponded with the reduced skill of these cases for near-bottom salinity, velocity, and bottom stress. The finer grid, reduced turbulent mixing case ( $Ri_{st} = 0.10$ ) best represented the observed evolution of the salinity front, and the velocity and bottom stress distributions, during this ebb and more generally over the observation period. In this case, the velocity structure corresponded with the salinity field, with strong shear across the pycnocline, ebbing velocities in the surface layer and near-zero velocities within  $\sim 1$  m above the bed. Comparison among the cases indicate that both grid size and turbulence closure affect the total mixing, and thus salinity fronts, so we examine the relative contributions of the turbulent and the numerical mixing.

### 3.3. Numerical and Turbulent Mixing

To assess the extent to which the mixing in the model, both implicit numerical and explicit turbulent, is consistent with mixing in the estuary, we examine frontal zone 4 at times corresponding with intensive field measurements of turbulence and mixing (Figure 7). The observations and data analysis are detailed in *Holliman et al.* [2016]. Here we focus on the calculations of dissipation of scalar variance ( $\chi_s$ ) from microconductivity sensors and acoustic Doppler velocimeters at multiple elevations. The dissipation of scalar variance is

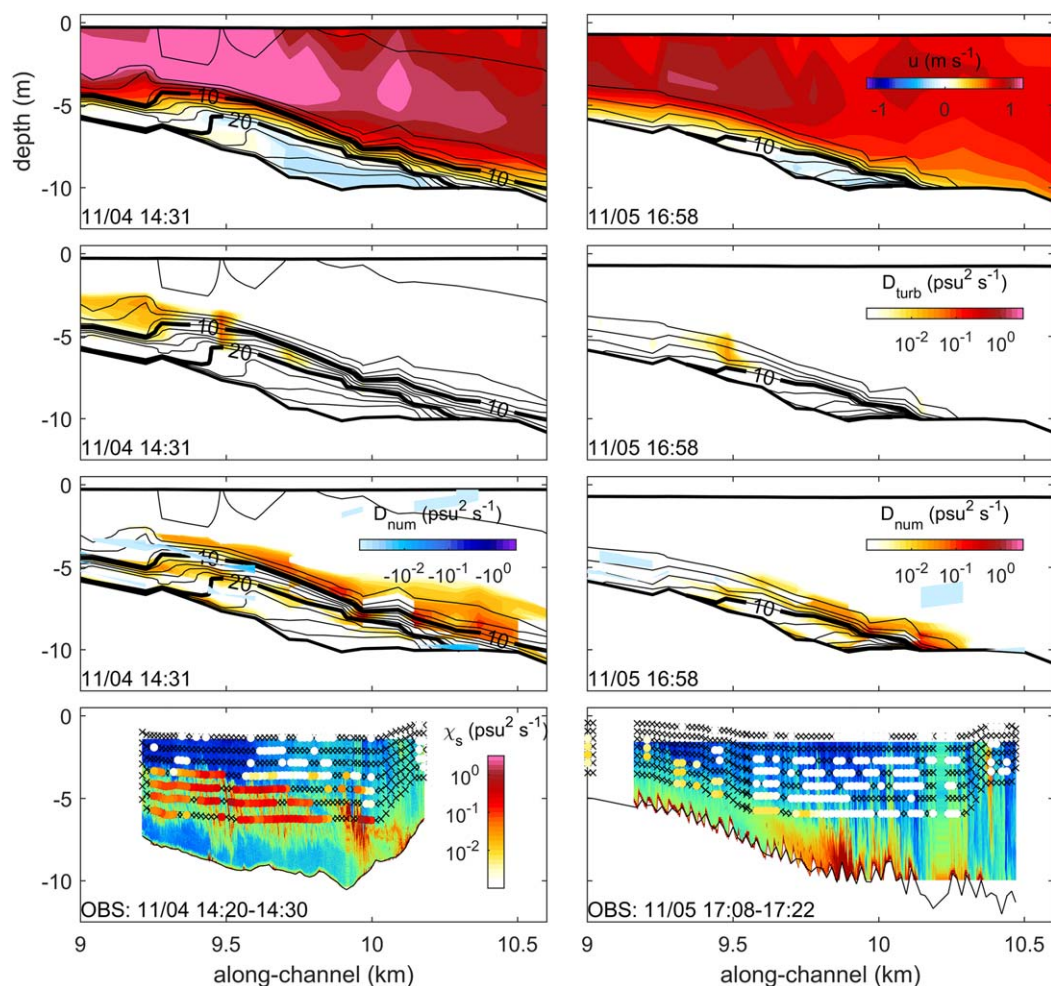


**Figure 7.** Along-channel sections of velocity and mixing in frontal zone 4 from the model and observations. (top row) Along-channel velocity (model), (second row)  $D_{turb}$  (model), (third row)  $D_{num}$  (model), all fine grid and  $Ri_{st} = 0.10$ . (fourth row) Corresponding observations on 4 and 5 November 2013 (adapted from Holleman *et al.* [2016]). In the observations, background colors represent broadband acoustic backscatter intensity (450–590 kHz). Colored dots show dissipation of scalar variance ( $\chi_s$ ) calculated from fast-response conductivity sensors and acoustic Doppler velocimeters at multiple levels. Black “x” marks are samples where the inertial range of the turbulence spectrum was not adequately resolved.

analogous to the dissipation of turbulent kinetic energy (TKE), in that to first-order the destruction of gradients at small scales by molecular diffusion (or viscosity for TKE) is balanced by the production of variance at large scales. In addition to the microconductivity sensors, broadband acoustic backscatter profiles provide more a continuous picture of the stratified turbulence. In regions of intense turbulence, salinity, and temperature microstructure create acoustic impedance gradients that cause intense scattering of high-frequency acoustic energy. Using a broadband acoustic array to resolve the spectral slope, Lavery *et al.* [2013] showed in observations from the Connecticut River that acoustic backscatter intensity can be used to estimate the dissipation of salinity variance. Although not as sensitive as the in situ microstructure measurements, acoustic backscatter provides high-spatial resolution of the variations in mixing within frontal zones with strong gradients.

Mid-ebb and late-ebb transects are shown for sequential days (4–5 November) from the observations and the model results with the fine grid and  $Ri_{st} = 0.10$  (Figure 7). Early in the ebb, the pycnocline was strongly sheared, with flow seaward at  $>1 \text{ m s}^{-1}$  in the surface layer and flow weakly landward below. Corresponding with the shear layer,  $D_{turb}$  was significant in the pycnocline, particularly toward the seaward end of the frontal zone. Numerical mixing occurred in the pycnocline as well, at levels similar to or greater than the turbulent mixing. The numerical contribution was greater than the turbulent toward the landward end of the

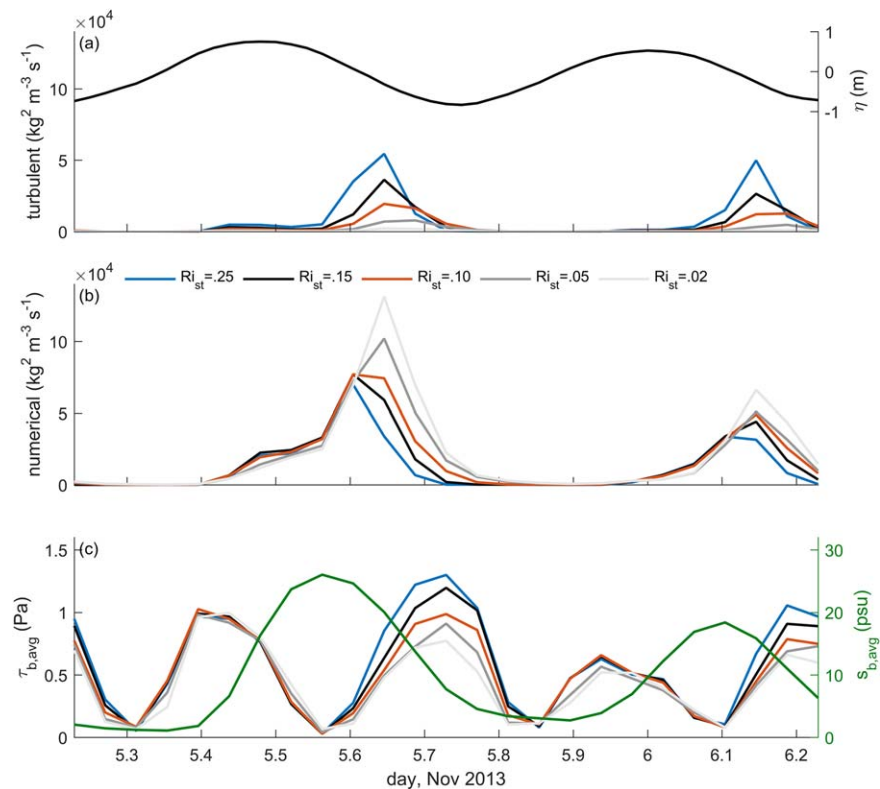


**Figure 8.** Volume integrated mixing and average bed stress in frontal zone 4 on 5 November 2013; the ebb from 5.55 to 5.85 d is also shown in Figures 7 and 8. (a) Volume integrated turbulent mixing over two tidal cycles for the fine grid with  $Ri_{st} = 0.25, 0.15, 0.10, 0.05,$  and  $0.02$ ; water level is on the right axis. (b) Volume integrated numerical mixing in frontal zone 4 for the same cases. (c) Average bottom stress in frontal zone 4 for the same cases, with average bottom salinity in green and on the right axis.

frontal zone where the pycnocline intersected the bed. The numerical mixing was also intense earlier in the ebb, when the landward limit of the front intersected the upward sloping bed (not shown). Advection of mixed water from this region of elevated  $D_{num}$  resulted in the more diffuse pycnocline in the model results early in the ebb than was seen in the observations (Figure 6, column 1).

While the total mixing in this case was dominated by the numerical contribution due to the calibration approach, the sum of the numerical and turbulent mixing corresponded spatially and temporally with the mixing found in the observations. In particular, during mid-ebb the mixing was concentrated in the pycnocline where observations indicate the occurrence of shear instabilities. Additional mixing was inferred from the acoustic backscatter at the base of the front that was not resolved by the microconductivity measurements. Later in the ebb, the mixing had moved down in the water column and was most intense where the pycnocline intersected the bed. In the model, the decay of salinity variance was primarily driven by the numerical diffusion rather than the turbulence closure, but the location of the numerical mixing coincided with the same regions of intense turbulent mixing as in the observations.

The total mixing in the frontal zone, including shallower regions as well as the thalweg, was dominated by mixing during ebbs (Figure 8). Turbulent mixing was negligible during much of the flood, and numerical mixing increased late in the flood when the surface layer began to ebb but the lower layer (and thus bottom stress) continued to be flood-oriented. Differences between the turbulence closure cases were most apparent during ebbs, as the contribution of turbulent mixing decreased with decreasing  $Ri_{st}$ . Correspondingly, the numerical mixing increased as the advection scheme acted on stronger salinity gradients that had not been mixed by turbulence. The net effect of reducing  $Ri_{st}$  was to delay the total mixing in the frontal zone, allowing the stratification to persist longer during the ebb, consistent with the observations. The delayed mixing affected the average bottom stress in the frontal zone, which decreased by almost a factor of 2 between the  $Ri_{st} = 0.25$  and  $Ri_{st} = 0.02$  cases (Figure 8).

**Table 3.** Fractional Mixing in the Fine Grid Cases for Salt (and Suspended Sediment for  $Ri_{st} = 0.10$ ) in Frontal Zone 4 and the Entire Estuary

$D_{num}/(D_{num} + D_{turb})$	$Ri_{st}$					
	0.25		0.15		0.10	
	Salt	Salt	Salt	Sediment	Salt	Salt
In frontal zone 4	0.59	0.74	0.82	0.36	0.93	0.98
In estuary	0.50	0.60	0.69	0.21	0.84	0.94

Integrated over these two tidal periods, numerical mixing in the  $Ri_{st} = 0.25$  case accounted for 50% of the total mixing of salt in the estuary, and 59% of the mixing in frontal zone 4 (Table 3). Reducing  $Ri_{st}$  increased the fractional contribution of numerical mixing to the total, but as noted above, improved the model skill for bottom salinity and velocity and had a spatial distribution of total mixing (numerical plus turbulent) that was consistent with turbulent mixing observations (Figure 7). For the case with  $Ri_{st} = 0.10$ , numerical mixing of salt was 69% of the total in the estuary and 82% in frontal zone 4. The distribution between numerical and turbulent mixing did not vary substantially with tidal or river forcing, as over a month-long simulation the numerical contribution ranged between 63% and 78% of the total.

Frontal zone 4 is but one of five regions in which bottom salinity fronts form downstream of constrictions during ebbs, and similar processes occurred in the other frontal zones. Strongly sloping bathymetry and strong horizontal salinity gradients enhanced numerical mixing in the frontal zones (Figure 9). Both the bed slopes and salinity gradients were exceptionally large compared to most conditions in the coastal or open ocean, exceeding 0.1 m/m and 0.1 psu/m in many locations. The greatest numerical mixing occurred at curving, steeply sloped banks where bottom salinity fronts intersected with the bed, particularly in frontal zones 2, 4, and 5. Turbulent mixing tended to be more broadly distributed and less intense than the numerical, but with focal areas at the edges of channels and in the seaward parts of frontal zones.

To evaluate their relative contributions over a longer period, the turbulent and numerical mixing were bin averaged as a function of distance along the estuary and salinity over a spring-neap cycle with moderate discharge (2–15 November, 2013,  $Q_{r,avg} = 290 \text{ m}^3 \text{ s}^{-1}$ ) (Figure 10). Turbulent mixing tended to be greatest in the downstream parts of the frontal zones, while numerical mixing was concentrated at the upstream end where the pycnocline intersected the bed. The turbulent mixing was more broadly distributed in salinity space, reflecting boundary layer mixing and weaker stratification after the salinity fronts had broken down. In contrast, numerical mixing was concentrated at the intermediate salinities of the pycnocline. In the observations, shear instabilities at the pycnocline dominated mixing in the early and middle ebb [Holliman *et al.*, 2016], and the numerical mixing in the model appears to be accounting for some of that. Additionally, horizontal mixing by physical processes at the scales of the grid spacing are not represented explicitly in these model cases with  $K_h = 0$ . Without explicit horizontal mixing, the numerical mixing may be smoothing horizontal gradients that otherwise would be mixed by unresolved horizontal processes. Physical horizontal mixing would be greatest in regions with sharp horizontal salinity gradients and lateral shear, which is also where the numerical mixing was most intense.

### 3.4. Pressure Gradient Error

Numerical errors due to the representation of internal pressure gradients in sigma-coordinate systems with steeply sloping bathymetries are well documented [Mellor *et al.*, 1994; Ezer *et al.*, 2002; Shchepetkin and McWilliams, 2003]. To evaluate the role of the internal pressure gradient error on numerical mixing, the model was run with no external forcing (rivers, tides, or wind) and an initial salinity distribution of uniform linear stratification of 0 to 30 psu from 3 to 6 m below the surface, representative of conditions in frontal zones during ebbs. Note that this persistent, strong stratification represents a worst-case scenario, as stratification in the Connecticut, as in most estuaries, is weaker for at least part of the tidal cycle. In the estuary in the finer grid case, the heterogeneous bathymetry induced internal pressure gradient errors and resulted in horizontal velocities that averaged  $0.033 \text{ m s}^{-1}$ . The maximum volume integrated numerical mixing due to the pressure gradient error was  $2 \times 10^4 \text{ kg}^2 \text{ m}^{-3} \text{ s}^{-1}$  in frontal zone 4 after about 3 h, decreasing to  $4 \times 10^3 \text{ kg}^2 \text{ m}^{-3} \text{ s}^{-1}$  after 24 h as the salinity gradients weakened. The velocities induced by the pressure gradient error were small, so the physical mixing calculated from the turbulence closure was more than an order

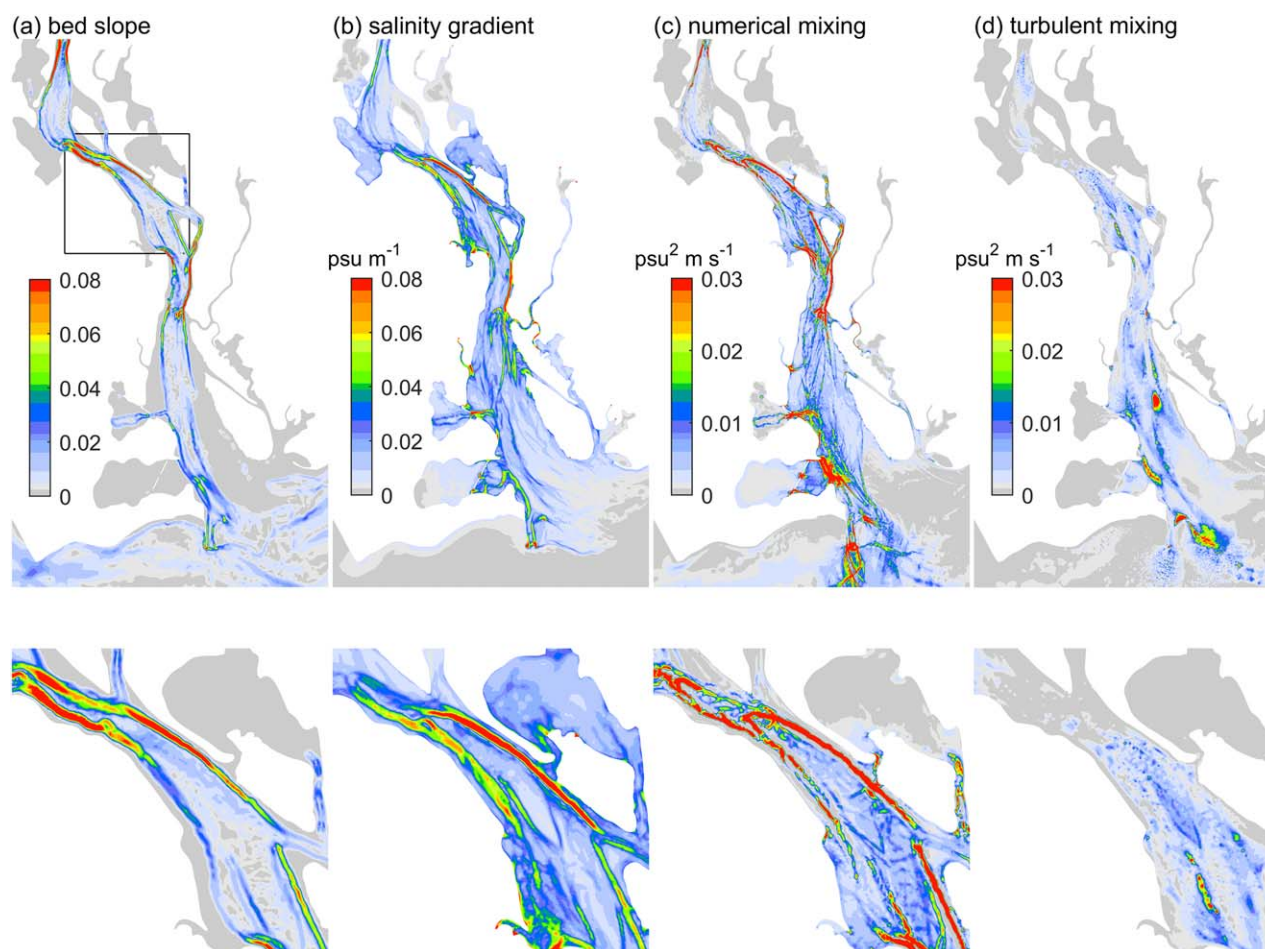


**Figure 9.** Spatial distribution of numerical and turbulent mixing averaged over two tidal cycles (5–6 November, as in Figure 8). (a) Bed slope, (b) average bottom salinity gradient over this period, (c) depth-averaged and time-averaged numerical mixing, (d) depth-averaged and time-averaged numerical mixing. Bottom plots show zoom-ins on frontal zone 4.

of magnitude less than the numerical mixing. Simulations with the same configuration for the coarse grid produced velocities of similar magnitude (average of  $0.028 \text{ m s}^{-1}$ ) and with numerical mixing rates that were about 2 times greater than those of the finer grid.

For comparison, the fine grid with tidal and river forcing had maximum values for the volume integrated numerical mixing in frontal zone 4 of about  $8 \times 10^4 \text{ kg}^2 \text{ m}^{-3} \text{ s}^{-1}$  (Figure 8,  $Ri_{st} = 0.25$ ), about 4 times that of the unforced case. This increase in mixing with external forcing indicates that the strongly advective regime due to the tidal and fluvial forcing significantly enhances the numerical mixing. The numerical mixing in the unforced case was substantial however, reflecting the interaction of the strong salinity gradient and topographic slope. An unforced case with weaker initial stratification (0–24 psu from the surface to 15 m depth) had much lower pressure gradient errors, with maximum volume integrated numerical mixing in frontal zone 4 of  $4 \times 10^3 \text{ kg}^2 \text{ m}^{-3} \text{ s}^{-1}$ , almost an order of magnitude less than the case with stronger initial stratification.

### 3.5. Bottom Stress and Sediment Transport

In addition to salinity, coastal circulation models are often used to represent the distribution of nutrients, organisms, contaminants, or sediment. In this application, the model development was driven in part to examine interactions between the salinity fronts and sediment transport. Sediment resuspension and transport depend greatly on bottom stress and near-bottom velocity, and the salinity distribution affects these through spatial gradients in stratification and velocity. The excessive mixing of salt in the fine grid case with  $Ri_{st} = 0.25$  resulted in average seaward bottom stresses in frontal zone 4 that were about 50% greater than the case with  $Ri_{st} = 0.10$  (Figure 8). The discrepancies in bottom stress however were not uniform, but

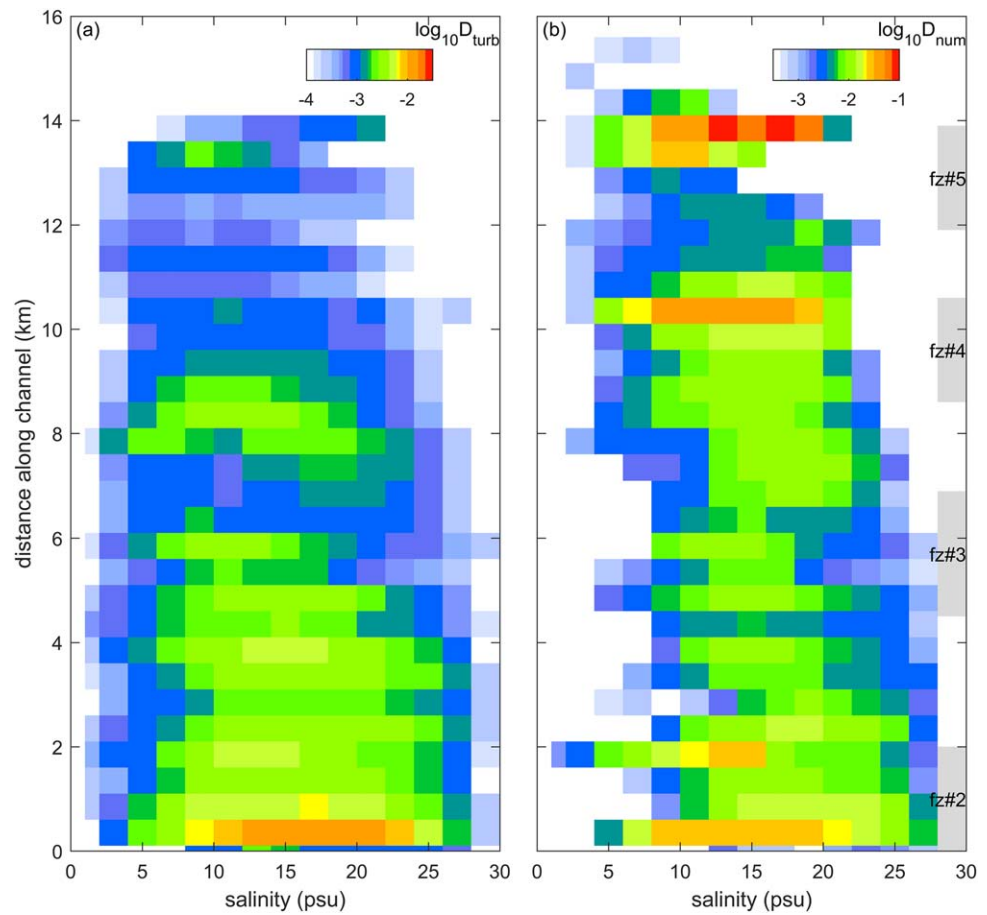


**Figure 10.** Turbulent and numerical mixing bin averaged by distance along the estuary and salinity for the fine grid,  $Ri_{st} = 0.10$  case. (a) Average turbulent mixing ( $\log_{10}$  of  $(\text{kg m}^{-3})^2 \text{s}^{-1}$ ) in spatial (distance from the mouth) and salinity bins over a spring-neap cycle (2–15 November 2013). (b) The same for average numerical mixing; note the difference in color scale. Frontal zone locations are noted on the right of Figure 10b.

corresponded with the location of the bottom salinity front (Figure 11). Bottom stresses for the  $Ri_{st} = 0.10$  case were similar to the  $Ri_{st} = 0.25$  case except in the channel at the upstream end of the frontal zone that remained stratified at the end of the ebbs. These are potential regions of sediment trapping, and the

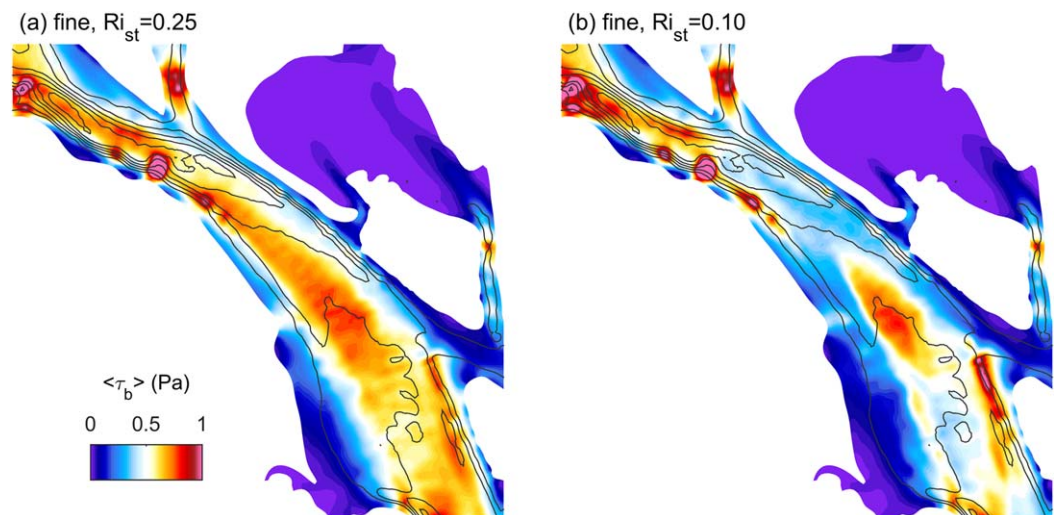


**Figure 11.** Bottom stress in frontal zone 4 averaged over two tidal periods (as in Figure 9). (a) Finer grid with  $Ri_{st} = 0.25$ ; (b) finer grid with  $Ri_{st} = 0.10$ . Black contour lines are bathymetry at 2 m intervals.

asymmetries in stress and sediment resuspension that have been observed in field studies were only reproduced in the fine grid model cases with reduced turbulent mixing.

Numerical mixing of suspended sediment also occurs due to advection of the spatial gradients, as with any scalar field. The numerical mixing of suspended sediment can be quantified in the same manner as salt (equation (2)) and compared with the vertical mixing of sediment by the turbulence closure. For the cases presented here, the numerical mixing contributed a much smaller fraction of the total mixing of suspended sediment than for salt (Table 3). For the fine grid case with  $Ri_{st} = 0.10$ , numerical mixing contributed 36% of the total mixing of suspended sediment in frontal zone 4 and 21% of the mixing in the estuary as a whole. Suspended sediment was less affected by advective dissipation because the horizontal gradients were weaker and they did not necessarily correspond with regions of strong velocity shear, as was the case for a dynamically active scalar like salt.

#### 4. Summary and Discussion

Development of a high-resolution model of the Connecticut River estuary combined high-resolution observations with a multiparameter calibration approach to produce simulations with improved skill. Both the fine and coarse model grids performed well in comparisons with water level and depth-averaged velocity after calibration of  $z_0$ , but the coarser grid required a  $z_0$  about 50% greater than the finer grid to compensate for unresolved flow structure. However, near-bottom salinity and velocity in frontal regions had lower model skill, as numerical mixing in regions of strong horizontal gradients was similar to the explicitly imposed mixing from the turbulence closure and led to excessive total mixing of salt. The combination of numerical and turbulent mixing eroded the stratification in frontal zones during ebbs faster than was observed, and consequently the near-bottom velocities had the wrong sign and magnitude. The limitations in the model were only identified through comparisons with high-resolution field data that characterized the strong gradients and rapidly evolving flow fields.

To compensate for the excessive numerical mixing, the turbulent mixing was reduced through adjustment of  $Ri_{st}$ . The optimal  $Ri_{st}$  for the fine grid ( $Ri_{st} = 0.10$ – $0.15$ ) were greater than for the coarse grid ( $Ri_{st} = 0.02$ ), consistent with the greater numerical mixing in the coarse grid. This trend suggests that an even greater resolution grid—perhaps 5 m in the estuary—could converge toward an optimal  $Ri_{st}$  around 0.25, more consistent with the physical gradient Richardson number in a homogenous stratified shear layer. Increasing the number of sigma levels from 30 to 40 did not significantly change the model results or skill, although we did not rigorously assess the sensitivity of the numerical mixing to vertical resolution. A general approach suggested by these results is that the calibration of coastal and estuarine numerical models should concurrently account for the effects of grid resolution, bottom boundary friction on barotropic dynamics (through  $z_0$ ), and internal mixing on the stratification (through the turbulence closure, in this case with the parameter  $Ri_{st}$ ). The factors are intrinsically coupled, so changes to any of them require recalibration of the others. The approach taken here should be applied with caution, as it may be not be appropriate in systems with low rates of physical mixing [Gräwe *et al.*, 2015].

In physical and salinity space, there were strong similarities in where the numerical and turbulent mixing occurred, as both increased in regions with enhanced velocities and salinity gradients (Figures 8 and 10). Similarly, the improved skills for salinity and stratification with the decrease in turbulent mixing and corresponding increase in numerical mixing as  $Ri_{st}$  was lowered indicates that the total mixing was better represented with decreased turbulent mixing. The numerical and turbulent mixing were coupled in that reducing turbulent mixing maintained stronger stratification and allowed for additional numerical mixing, and vice versa as numerical mixing increased with grid spacing. In a study of the Faroe Bank Channel overflow using a structured grid, z-level numerical model, no turbulence closure scheme was needed to represent observed conditions due to the compensating effect of numerical mixing [Riemenschneider and Legg, 2007]. In that study, as was found here, the numerical mixing was sensitive to horizontal resolution, and to a lesser extent the vertical resolution.

The major contribution of numerical mixing to the total mixing in energetic, stratified flow environments confounds interpretation of turbulent fluxes calculated from the closure model. For example, model results from the Merrimack River estuary, a similar tidal salt wedge estuary, were used to calculate that  $1/2$  of the total buoyancy flux was due to internal shear layer turbulence, and that the overall turbulent mixing

efficiency in the estuary averaged about 0.05 [Ralston *et al.*, 2010b]. The results here suggest that numerical mixing likely contributed significantly to the buoyancy flux by mixing salt in high-gradient regions during ebbs, and the calculation based only on the turbulent buoyancy flux underestimated of the role of internal shear layer turbulence. Consequently, the actual mixing efficiency of the system may be considerably higher than the estimate of 0.05.

Unstructured grids have distinct advantages in coastal and estuarine settings with meandering shorelines and complex bathymetry, as grid resolution can be focused in regions of interest to resolve spatial structure. The wide range of relevant forcing scales for this system, from the  $\sim 100$  km domain for remote boundary forcing to the salinity gradients and stratified mixing processes in frontal zones at the scale of  $\sim 5$  m, make an unstructured grid a viable framework. A disadvantage of the unstructured approach is that it is more difficult to implement higher order advection schemes than in rectangular or curvilinear grids, so they are more prone to the numerical mixing due to truncation of the higher order terms. Numerical mixing depends not only on grid resolution and advection scheme, but also the scalar gradients (no numerical mixing if the scalar field is uniform) and the velocity field (no numerical mixing if the velocities are zero). Estuaries, and in particular energetic, highly stratified estuaries like the Connecticut, present challenges with strong velocities, stratification, and horizontal salinity gradients.

With unlimited computational resources, the simplest solution would be to continue to add grid resolution to represent the spatial gradients in bathymetry and salinity. However, resources are limited in practice, so the goal instead is to optimize the model setup to create simulations that represent the real world with quantifiable skill and that can then be analyzed for physical processes. Here we had particularly high-resolution observations with which to identify model errors in stratification and near-bottom velocity, and found that the fine grid model that was feasible for this application had excessive numerical mixing. To compensate, we reduced  $Ri_{st}$  and the turbulent mixing until the total mixing in the estuary better matched the observed salinity structure. In larger, more coarsely resolved estuaries the opposite may be true, for example if unresolved mixing processes are not explicitly part of the model formulation (e.g., breaking internal waves) and weak salinity and bathymetric gradients make numerical mixing less problematic. In those coarser models, the turbulent mixing may be calibrated to allow for more mixing than strictly dictated by the expected physical value for  $Ri_g$ , by increasing  $Ri_{st}$  or choosing stability coefficients with a greater  $Ri_{cr}$ .

The total mixing, numerical and turbulent, determines the bulk characteristics of the estuary such as salinity, velocity, stratification, and bed stress, and yet it remains difficult to determine a priori the turbulence closure parameters as they are coupled to the numerical mixing due to advection, which is poorly constrained in most circulation models. In these results, the reduction of  $Ri_{st}$  seems to be a reasonable approach because measurements of turbulent mixing correspond quantitatively with the total mixing in the model, the numerical contribution plus the turbulence closure. Whether this is a generally applicable approach for coastal models to mitigate excessive numerical mixing remains to be determined. In general, the role of numerical mixing remains largely unknown or unacknowledged for most realistic applications, for both unstructured and structured grids. A more methodical and comprehensive study of the tradeoffs in modeling approaches—structured or unstructured, advection scheme order, vertical coordinate system—using a quantitative assessment of the numerical mixing in realistic applications would provide welcome guidance for the community of coastal and estuarine model users.

#### Acknowledgments

Support for this study was provided by NSF grant OCE 0926427 (DKR, WRG, RCH) and ONR grant N00014-08-1-1115 (GWC). The authors thank Hans Burchard for helpful discussions. The observational data, model results, and model code from this study are available from David Ralston (dralston@whoi.edu).

#### References

- Ackerman, S. D., D. S. Foster, E. M. Moore, B. J. Irwin, and D. S. Blackwood (2015), *High-Resolution Geophysical and Sampling Data Collected at the Mouth of Connecticut River*, Old Saybrook to Essex, 2012, USGS Field Activ., Woods Hole, Mass.
- Allen, J. R. (1970), *Physical Processes of Sedimentation*, Am. Elsevier Publ. Co., Allen and Unwin, London.
- Bokuniewicz, H. J., R. B. Gordon, and K. A. Kastens (1977), Form and migration of sand waves in a large estuary, Long Island Sound, *Mar. Geol.*, *24*(3), 185–199.
- Burchard, H. (2001), On the  $q_2l$  Equation by Mellor and Yamada (1982), *J. Phys. Oceanogr.*, *31*(5), 1377–1387.
- Burchard, H., and K. Bolding (2001), Comparative analysis of four second-moment turbulence closure models for the oceanic mixed layer, *J. Phys. Oceanogr.*, *31*(8), 1943–1968.
- Burchard, H., and H. Rennau (2008), Comparative quantification of physically and numerically induced mixing in ocean models, *Ocean Modell.*, *20*(3), 293–311, doi:10.1016/j.ocemod.2007.10.003.
- Canuto, V. M., A. Howard, Y. Cheng, and M. S. Dubovikov (2001), Ocean turbulence. Part I: One-point closure model—Momentum and heat vertical diffusivities, *J. Phys. Oceanogr.*, *31*(6), 1413–1426.
- Chen, C., H. Liu, and R. C. Beardsley (2003), An unstructured grid, finite-volume, three-dimensional, primitive equations ocean model: Application to coastal ocean and estuaries, *J. Atmos. Oceanic Technol.*, *20*(1), 159–186.

- Chen, C., H. Huang, R. C. Beardsley, H. Liu, Q. Xu, and G. Cowles (2007), A finite volume numerical approach for coastal ocean circulation studies: Comparisons with finite difference models, *J. Geophys. Res.*, *112*, C03018, doi:10.1029/2006JC003485.
- Chen, C., J. Qi, C. Li, R. C. Beardsley, H. Lin, R. Walker, and K. Gates (2008), Complexity of the flooding/drying process in an estuarine tidal-creek salt-marsh system: An application of FVCOM, *J. Geophys. Res.*, *113*, C07052, doi:10.1029/2007JC004328.
- Chen, C. et al. (2013), *An Unstructured Grid, Finite-Volume Coastal Ocean Model: FVCOM User Manual*, 4th ed., Univ. of Mass., Dartmouth, Mass.
- Cheng, Y., V. M. Canuto, and A. M. Howard (2002), An improved model for the turbulent PBL, *J. Atmos. Sci.*, *59*(9), 1550–1565.
- Chua, V. P., and O. B. Fringer (2011), Sensitivity analysis of three-dimensional salinity simulations in North San Francisco Bay using the unstructured-grid SUNTANS model, *Ocean Modell.*, *39*(3), 332–350.
- Ezer, T., H. Arango, and A. F. Schepetkin (2002), Developments in terrain-following ocean models: Intercomparisons of numerical aspects, *Ocean Modell.*, *4*(3), 249–267.
- Geyer, W. R., and D. M. Farmer (1989), Tide-induced variation of the dynamics of a salt wedge estuary, *J. Phys. Oceanogr.*, *19*(8), 1060–1072.
- Geyer, W. R., and P. MacCready (2014), The estuarine circulation, *Annu. Rev. Fluid Mech.*, *46*(1), 175–197, doi:10.1146/annurev-fluid-010313-141302.
- Geyer, W. R., and D. K. Ralston (2015), Estuarine frontogenesis, *J. Phys. Oceanogr.*, *45*(2), 546–561.
- Giddings, S. N., D. A. Fong, S. G. Monismith, C. C. Chickadel, K. A. Edwards, W. J. Plant, B. Wang, O. B. Fringer, A. R. Horner-Devine, and A. T. Jessup (2011), Frontogenesis and frontal progression of a trapping-generated estuarine convergence front and its influence on mixing and stratification, *Estuaries Coasts*, *35*(2), 665–681, doi:10.1007/s12237-011-9453-z.
- Gräwe, U., P. Holtermann, K. Klingbeil, and H. Burchard (2015), Advantages of vertically adaptive coordinates in numerical models of stratified shelf seas, *Ocean Modell.*, *92*, 56–68, doi:10.1016/j.ocemod.2015.05.008.
- Holleman, R., O. Fringer, and M. Stacey (2013), Numerical diffusion for flow-aligned unstructured grids with application to estuarine modeling, *Int. J. Numer. Methods Fluids*, *72*(11), 1117–1145.
- Holleman, R. C., W. R. Geyer, and D. K. Ralston (2016), Stratified turbulence and mixing efficiency in a salt wedge estuary, *J. Phys. Oceanogr.*, *46*(6), 1769–1783, doi:10.1175/JPO-D-15-0193.1.
- Horne, G. S., and P. C. Patton (1989), Bedload-sediment transport through the Connecticut River estuary, *Geol. Soc. Am. Bull.*, *101*(6), 805–819.
- Huang, H., C. Chen, G. W. Cowles, C. D. Winant, R. C. Beardsley, K. S. Hedstrom, and D. B. Haidvogel (2008), FVCOM validation experiments: Comparisons with ROMS for three idealized barotropic test problems, *J. Geophys. Res.*, *113*, C07042, doi:10.1029/2007JC004557.
- Hubbard, M. E. (1999), Multidimensional slope limiters for MUSCL-type finite volume schemes on unstructured grids, *J. Comput. Phys.*, *155*(1), 54–74.
- Kantha, L. H., and C. A. Clayson (1994), An improved mixed layer model for geophysical applications, *J. Geophys. Res.*, *99*(C12), 25,235–25,266.
- Klingbeil, K., M. Mohammadi-Aragh, U. Gräwe, and H. Burchard (2014), Quantification of spurious dissipation and mixing—Discrete variance decay in a Finite-Volume framework, *Ocean Modell.*, *81*, 49–64, doi:10.1016/j.ocemod.2014.06.001.
- Knebel, H. J., R. P. Signell, R. R. Rendigs, L. J. Poppe, and J. H. List (1999), Seafloor environments in the Long Island Sound estuarine system, *Mar. Geol.*, *155*(3), 277–318.
- Kobayashi, M. H., J. M. Pereira, and J. C. Pereira (1999), A conservative finite-volume second-order-accurate projection method on hybrid unstructured grids, *J. Comput. Phys.*, *150*(1), 40–75.
- Lai, Z., R. Ma, G. Gao, C. Chen, and R. C. Beardsley (2015), Impact of multichannel river network on the plume dynamics in the Pearl River estuary, *J. Geophys. Res. Oceans*, *120*, 5766–5789, doi:10.1002/2014JC010490.
- Lavery, A. C., W. R. Geyer, and M. E. Scully (2013), Broadband acoustic quantification of stratified turbulence, *J. Acoust. Soc. Am.*, *134*(1), 40–54, doi:10.1121/1.4807780.
- Li, L., H. Wu, J. T. Liu, and J. Zhu (2014), Sediment transport induced by the advection of a moving salt wedge in the Changjiang estuary, *J. Coastal Res.*, 671–679, doi:10.2112/JCOASTRES-D-13-00186.1.
- Li, M., L. Zhong, and W. C. Boicourt (2005), Simulations of Chesapeake Bay estuary: Sensitivity to turbulence mixing parameterizations and comparison with observations, *J. Geophys. Res.*, *110*, C12004, doi:10.1029/2004JC002585.
- Mellor, G. L., T. Ezer, and L.-Y. Oey (1994), The pressure gradient conundrum of sigma coordinate ocean models, *J. Atmos. Oceanic Technol.*, *11*(4), 1126–1134.
- Miles, J. W. (1961), On the stability of heterogeneous shear flows, *J. Fluid Mech.*, *10*(04), 496–508.
- Murphy, A. H. (1988), Skill scores based on the mean square error and their relationships to the correlation coefficient, *Mon. Weather Rev.*, *116*(12), 2417–2424.
- Nash, J., and J. V. Sutcliffe (1970), River flow forecasting through conceptual models. Part I—A discussion of principles, *J. Hydrol.*, *10*(3), 282–290.
- Nikuradse, J. (1933), Laws of flow in rough pipes. VDI Forschungsheft 361, in translation, National Advisory Committee for Aeronautics Technical Memorandum 1292, 1950.
- Patton, P. C., and G. S. Horne (1992), Response of the Connecticut River estuary to late Holocene sea level rise, *Geomorphology*, *5*(3), 391–417.
- Ralston, D. K., W. R. Geyer, and J. A. Lerczak (2010a), Structure, variability, and salt flux in a strongly forced salt wedge estuary, *J. Geophys. Res.*, *115*, C06005, doi:10.1029/2009JC005806.
- Ralston, D. K., W. R. Geyer, J. A. Lerczak, and M. Scully (2010b), Turbulent mixing in a strongly forced salt wedge estuary, *J. Geophys. Res.*, *115*, C12024, doi:10.1029/2009JC006061.
- Ralston, D. K., W. R. Geyer, P. A. Traykovski, and N. J. Nidziko (2013), Effects of estuarine and fluvial processes on sediment transport over deltaic tidal flats, *Cont. Shelf Res.*, *60*, 540–557, doi:10.1016/j.csr.2012.02.004.
- Rennau, H., and H. Burchard (2009), Quantitative analysis of numerically induced mixing in a coastal model application, *Ocean Dyn.*, *59*(5), 671–687, doi:10.1007/s10236-009-0201-x.
- Riemenschneider, U., and S. Legg (2007), Regional simulations of the Faroe Bank Channel overflow in a level model, *Ocean Modell.*, *17*(2), 93–122, doi:10.1016/j.ocemod.2007.01.003.
- Rohr, J. J., E. C. Itsweire, K. N. Helland, and C. W. Van Atta (1988), Growth and decay of turbulence in a stably stratified shear flow, *J. Fluid Mech.*, *195*, 77–111.
- Schepetkin, A. F., and J. C. McWilliams (1998), Quasi-monotone advection schemes based on explicit locally adaptive dissipation, *Mon. Weather Rev.*, *126*(6), 1541–1580.
- Schepetkin, A. F., and J. C. McWilliams (2003), A method for computing horizontal pressure-gradient force in an oceanic model with a nonaligned vertical coordinate, *J. Geophys. Res.*, *108*(C3), 3090, doi:10.1029/2001JC001047.

- Simpson, J. H., and R. A. Nunes (1981), The tidal intrusion front: An estuarine convergence zone, *Estuarine Coastal Shelf Sci.*, *13*(3), 257–266, doi:10.1016/S0302-3524(81)80024-2.
- Smolarkiewicz, P. K. (1983), A simple positive definite advection scheme with small implicit diffusion, *Mon. Weather Rev.*, *111*(3), 479–486, doi:10.1175/1520-0493(1983)111 <0479:ASPDAS>2.0.CO;2.
- Stacey, M. T., and D. K. Ralston (2005), The scaling and structure of the estuarine bottom boundary layer, *J. Phys. Oceanogr.*, *35*(1), 55–71.
- Umlauf, L., and H. Burchard (2005), Second-order turbulence closure models for geophysical boundary layers. A review of recent work, *Cont. Shelf Res.*, *25*(7–8), 795–827, doi:10.1016/j.csr.2004.08.004.
- Umlauf, L., H. Burchard, and K. Hutter (2003), Extending the k-[omega] turbulence model towards oceanic applications, *Ocean Modell.*, *5*(3), 195–218, doi:10.1016/S1463-5003(02)00039-2.
- Vitousek, S., and O. B. Fringer (2011), Physical vs. numerical dispersion in nonhydrostatic ocean modeling, *Ocean Modell.*, *40*(1), 72–86.
- Wang, B., S. N. Giddings, O. B. Fringer, E. S. Gross, D. A. Fong, and S. G. Monismith (2011), Modeling and understanding turbulent mixing in a macrotidal salt wedge estuary, *J. Geophys. Res.*, *116*, C02036, doi:10.1029/2010JC006135.
- Warner, J. C., C. R. Sherwood, H. G. Arango, and R. P. Signell (2005), Performance of four turbulence closure models implemented using a generic length scale method, *Ocean Modell.*, *8*(1), 81–113.

### Erratum

In the originally published version of this article, in Equation 1, the numerator of the right side was " $A\{s^2\} - A\{s^2\}$ " when it should have been " $A\{s^2\} - A\{s\}^2$ ". This has since been corrected, and this version may be considered the authoritative version of record.